

NATIONAL BUREAU OF STANDARDS
MICROCOPY RESOLUTION TEST CHART

(2)

ESD-TR-84-295

AD-A158 013

Quarterly Technical Report

Solid State Research

1984:4

Lincoln Laboratory

MASSACHUSETTS INSTITUTE OF TECHNOLOGY

LEXINGTON, MASSACHUSETTS



Prepared under Electronic Systems Division Contract F19628-85-C-0002.

Approved for public release; distribution unlimited.

DTIC
ELECTE
JUL 2 9 1985

S

G

85 07 15 310

DTIC FILE COPY

114

The work reported in this document was performed at Lincoln Laboratory, a center for research operated by Massachusetts Institute of Technology, with the support of the Department of the Air Force under Contract F19628-85-C-0002.

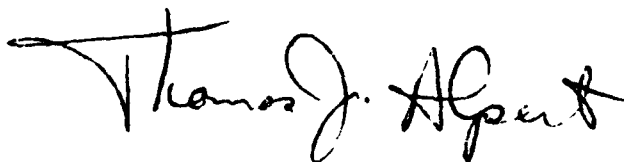
This report may be reproduced to satisfy needs of U.S. Government agencies.

The views and conclusions contained in this document are those of the contractor and should not be interpreted as necessarily representing the official policies, either expressed or implied, of the United States Government.

The ESD Public Affairs Office has reviewed this report, and it is releasable to the National Technical Information Service, where it will be available to the general public, including foreign nationals.

This technical report has been reviewed and is approved for publication.

FOR THE COMMANDER



**Thomas J. Alpert, Major, USAF
Chief, ESD Lincoln Laboratory Project Office**

Non-Lincoln Recipients

PLEASE DO NOT RETURN

**Permission is given to destroy this document
when it is no longer needed.**

MASSACHUSETTS INSTITUTE OF TECHNOLOGY
LINCOLN LABORATORY

SOLID STATE RESEARCH

QUARTERLY TECHNICAL REPORT

1 AUGUST — 31 OCTOBER 1984

ISSUED 28 FEBRUARY 1985

Approved for public release: distribution unlimited.

Accession For	
NTIS GRA&I	<input checked="" type="checkbox"/>
DTIC TAB	<input type="checkbox"/>
Unannounced	<input type="checkbox"/>
Justification	
By _____	
Distribution/	
Availability Codes	
Dist	Avail and/or Special
<i>A/</i>	



LEXINGTON

MASSACHUSETTS

ABSTRACT

This report covers in detail the solid state research work of the Solid State Division at Lincoln Laboratory for the period 1 August through 31 October 1984. The topics covered are Solid State Device Research, Quantum Electronics, Materials Research, Microelectronics, and Analog Device Technology. Funding is primarily provided by the Air Force, with additional support provided by the Army, DARPA, Navy, NASA, and DOE.



TABLE OF CONTENTS

Abstract	iii
List of Illustrations	vii
List of Tables	x
Summary	xi
Reports on Solid State Research Organization	xv xxv
1. SOLID STATE DEVICE RESEARCH	1
1.1 Lateral Photodetectors on Semi-insulating InGaAs and InP	1
1.2 Power Splitting Behavior of Optical Waveguide Struc- tures with Closely Spaced Abrupt Bends and Branches	4
1.3 Integrated Optics Wavefront Measurement Sensor	5
1.4 A Novel GaInAsP/InP Distributed Feedback Laser	7
1.5 Single-Mode InP Optical Waveguide Capable of Phase Modulation	12
2. QUANTUM ELECTRONICS	17
2.1 Evaluation of the Nd:Cr:GSGG Laser	17
2.2 Enhanced Quantum Efficiency Internal Photoemission Detectors by Grating Coupling to Surface Plasma Waves	20
2.3 Theory of the Effect of Traps on the Spectral Charac- teristics of Diode Lasers	23
3. MATERIALS RESEARCH	27
3.1 Impurities in Polycrystalline InP Ingots	27
3.2 Microwave MESFETs Fabricated in Zone-Melting- Recrystallized Si-on-Quartz Films	31
4. MICROELECTRONICS	35
4.1 Gallium Arsenide Charge-Coupled Devices	35
4.2 Picosecond GaAs PIN Photodiodes	38
4.3 Quantum Well Oscillators	39

5. ANALOG DEVICE TECHNOLOGY	43
5.1 Histogram Readout Technique for Charge-Coupled Image Processors	43
5.2 Wideband Suppression of Strong Signals in the Presence of Weak Signals by Bandpass-Limiter Cancellation	47

LIST OF ILLUSTRATIONS

Figure No.		Page
1-1(a)	Schematic Cross Section of InGaAs PSIN Structure. Gap Spacing (d) Is 3, 5, 10, or 20 μm .	2
1-1(b)	Curve Tracer I-V Characteristics of a 20- μm PSIN Device in Dark and Under Illumination	2
1-2	Pulse Response of a 3- μm PSIN Device, Under Forward and Reverse Bias, to a Comb-Generator-Driven InGaAsP Laser ($\lambda = 1.24 \mu\text{m}$). Notice Different Time Scales but Similar Peak Heights. FWHM Is 1.2 ns and 57.2 ps Under Forward and Reverse Bias, Respectively.	3
1-3	Measured Transmission from Two Branch Arms of Bend-Branch Structures Plotted vs Their Connecting-Segment Lengths. Measurements Were Made Using TM-Polarized Light at a Wavelength of 0.83 μm .	4
1-4	Wavefront Measurement Sensor Consisting of an Array of Interferometers with Horn Antennas as Input and CCD Imager as Output	5
1-5	Experimental Results $P_{\phi}(P)$ for an Array of 20 Interferometers Read Out from a CCD Imager Are Compared with Theoretical Curve $\cos^2(\phi/2)$. The More Than 500 Data Points Were Normalized so Maximum Value of Ratio for Each Interferometer Was Unity. Phase Angle ϕ for Experimental Points for Each Interferometer Was Adjusted by a Constant for Each Interferometer for Best Fit. Input Radiation Was at 810 nm.	6
1-6	A Schematic Drawing of the GaInAsP/InP Distributed Feedback Laser	7
1-7	Emission Spectra of One Device Just Above Lasing Threshold at (a) 20°C and (b) 10.6°C. In (a), Lasing Modes Are Shown Located on Shorter-Wavelength Side of Apparent Spontaneous Emission Spectrum. Expanded Wavelength Scale in (b) Shows More Details of Lasing Spectrum.	8
1-8	Emission Spectra of Device at 20.6°C and Two Different Currents Above Threshold. Note That, at $I = 1.54 I_{th}$, Sidemodes Are Lower Than -32 dB.	10

Figure No.		Page
1-9	Calculated Current and Voltage Distributions Near Active Region in Present Structure. Dashed Curves Are Streamlines of Current Flowing into Active Region. Solid Curves Are Equipotentials, with Numbers Labeling Voltage Values in Volts.	11
1-10	Schematic of Single-Mode p^+n-n^+ InP Slab-Coupled Rib Waveguide	12
1-11	Relative Output vs Reverse Bias of 5-mm-Long p^+n-n^+ InP Slab-Coupled Rib Waveguide with Approximately Equal Amounts of TE- and TM-Like Radiation Excited at Input and an Output Analyzer Parallel and Perpendicular to Input Polarization	13
2-1	Input-Output Energy Curves at 1060 nm for the Nd:Cr:GSGG Laser for Three Different Output-Mirror Transmissions	18
2-2	Thermal Lens Created by Pumped Nd:Cr:GSGG Rod as a Function of Average Power to Pump Lamp. Lamp Pulse Rate Was 10 Hz.	18
2-3	Input-Output Energy Curves for 1300-nm Operation of Nd:Cr:GSGG Laser, at Two Different Output-Mirror Transmissions	19
2-4	Reflectivity (Top) and Detector Response (Bottom) as Incident Angle Is Varied for TM-Polarized, 1.15- μm Radiation Incident on an Au-(p-InP) Schottky-Barrier Internal Photoemission Detector with an Etched Surface Grating (See Text for Details). Dips in Reflectivity and Corresponding Peaks in Response Occur at Angles for Coupling into Surface Plasma Waves at Air-Metal Interface.	21
2-5	Schematic Plot of FM Noise Spectrum of Diode Laser for Trap Model Discussed in Text. Solid Line Is Sum of Contributions Due to Fluctuations in Laser Phase and Amplitude (Designated by 1 and 2, Respectively). Dashed Line Is Total Spectrum Obtained by Adding Contributions of Traps Designated as μ and d .	25
3-1	Distribution of Electron Hall Mobilities at 77 K for Polycrystalline InP Ingots	29
3-2	Schematic Diagram and Photomicrograph of Si-on-Quartz Microwave MESFET	32
3-3	Drain I-V Characteristics of SOQ MESFET	33
3-4	Maximum Available Gain as a Function of Frequency for SOQ MESFET	34

Figure No.		Page
4-1	Fabrication Sequence of GaAs Overlapping Gate CCD	36
4-2	Scanning Electron Micrograph of Overlapping CCD Gates	36
4-3	CCD Input (Top) and Output (Bottom) for (a) 6-V and (b) 4-V Clock Amplitude	37
4-4	Photomicrograph of p-i-n Device. Width of Electrodes Is 100 μm . This Device Was Designed as an RF Switch for Microwave and Millimeter-Wave Applications.	38
4-5	Current-Voltage Characteristic for a Quantum Well Resonator. Dark Line Is True Curve for a Stable Device; Light Line Was Measured When Oscillating at 4 GHz. Difference Is Due to Self-Detection.	40
4-6	Spectrum of Oscillating Quantum Well Resonator. Wings Below -60 dBm Which Extend to a Few Megahertz Are Probably Due to Low-Frequency Noise in Charge Transport Process.	40
5-1	Example of a CCD Structure for Performing Histogram Readout	44
5-2	Drive Waveform on Storage Gate G_s and Output Current I_D on Common Diffusion D During Operation of Histogram Readout Device	44
5-3	Charge-Storage and Flow Patterns at Times a Through e Shown in Figure 5-2	45
5-4	Experimental Demonstration of Histogram Readout from a 32-Well Demonstration Device for a Steady (a) and Shifting (b) Triangular Image Pattern. Upper Trace Is Voltage on G_s ; Middle Trace Shows Stored Charge Pattern (Increasing Downward); and Bottom Trace Shows Current on Common Diffusion D.	46
5-5	Larger (Nearer) Signal-Suppression Circuit	49
5-6	Near/Far Signal Suppression Results with Two Wideband Input Signals. Output of Convolver Matched Filter Is Shown. (a) Output of Convolver with Bandpass-Limiter Path Disabled and Direct Path Enabled. (b) Output with Bandpass-Limiter Leg Enabled and Direct Path Disabled. (c) Output with Both Circuit Paths Enabled. "Near" Signal and Its Side Lobes Are Clearly Suppressed.	50

Figure No.		Page
5-7	Multiple Near/Far Suppression Results. (a) Output for Large and Two Successively Smaller and Delayed Signals. (b) Output After a Single Stage of Near/Far Suppression. (c) Output After Two Stages of Near/Far Suppression.	51
5-8	Narrowband Near/Far Suppression Results. (a) Spectrum of Signal Showing Large and Small Narrowband Signals. Bandpass-Limiter Path Is Disabled. (b) Spectrum of Signal with Both Paths Enabled. Large Tone Is Clearly Suppressed.	52

LIST OF TABLES

Table No.		Page
3-1	Synthesis Parameters and Electrical Properties of Polycrystalline InP Ingots Prepared in 1984	28
3-2	Concentrations of Si Found by SIMS Analysis	31

SUMMARY

1. SOLID STATE DEVICE RESEARCH

A new type of high-performance lateral PIN photodetector has been formed by alloying p- and n-type metallic contacts onto semi-insulating InGaAs or InP without a separate junction fabrication step. Low dark current (<1 nA), high external quantum efficiency (40% at $\lambda = 1.24$ μm , without antireflection coating), and high speed (FWHM < 50 ps) have been obtained with reverse bias of 10 V. These characteristics, plus the simplicity of fabrication and the planar lateral configuration, make these devices attractive for photodetector arrays and for monolithic integration with field-effect transistors.

Optical waveguide structures with symmetric branches preceded by abrupt bends have been studied. Measured power-splitting ratios range from 0 to 6 dB and oscillate with the bend-branch separation. The power splitting also depends on the mode effective index, which is affected by the polarization, wavelength, and waveguide fabrication parameters.

The performance evaluation of the components for the integrated optics wavefront measurement sensor is continuing. The experimental results, obtained when the interferometer array output is coupled into and then read out of a CCD imager, show excellent agreement with theory.

GaInAsP/InP distributed feedback lasers have been fabricated with a simple new design in which the grating is etched into the top of a mass-transported buried heterostructure. Single-frequency operation with sidemodes lower than -32 dB and threshold currents as low as 16 mA has been achieved.

Single-mode InP p^+n-n^+ slab-coupled rib waveguides capable of phase modulating, TE-polarized, 1.3- μm radiation have been fabricated. These guides should prove useful in the fabrication of two-guide coupler switches and interferometric modulators.

2. QUANTUM ELECTRONICS

The Nd:Cr:GSGG solid state laser has been investigated. Operation at 1060 nm shows an improvement by nearly a factor of two in slope efficiency over Nd:YAG at the expense of a much greater thermal-lensing effect. High-efficiency operation at 1300 nm also has been demonstrated.

Enhanced quantum efficiencies have been obtained for Au-InP internal photoemission detectors using grating coupling of incident radiation into surface plasma waves confined to the air-metal interface. Enhancements of over a factor of 30 have been obtained at the resonance coupling angles. Time-resolved response measurements show that the present detectors are RC-limited, and response speeds under 10 ps are attainable with lower carrier concentration materials and smaller active areas.

3. MATERIALS RESEARCH

The yield of high-purity InP ingots synthesized from the elements during the past year was significantly lower than in previous years, a decrease that can be attributed to the continuing low purity of as-received phosphorus and a reduction in the effectiveness with which electrically active impurities were removed (or rendered inactive) by prebaking the phosphorus before synthesis. Since secondary-ion mass spectrometric (SIMS) analysis of ingots with carrier concentrations exceeding $1 \times 10^{16} \text{ cm}^{-3}$ shows that Si is the dominant donor impurity, it is probable that as-received phosphorus is contaminated with Si. If not, the phosphorus must contain some other impurity that influences the incorporation of Si from another source into the InP.

Microwave MESFETs with promising performance have been fabricated in zone-melting-recrystallized Si films on fused-silica substrates. The Si-on-quartz structure should be useful for monolithic microwave integrated circuits because of its low parasitic capacitance and the low dielectric loss of quartz.

A theory of the effect of traps on diode laser characteristics has been formulated to explain (1) the excess linewidth, and (2) the $1/f$ components in the FM and current fluctuation spectra of GaAs/GaAlAs double-heterostructure lasers. The theory attributes these phenomena to fluctuations in the populations of traps located in the active region and in the GaAlAs confining layers, respectively.

4. MICROELECTRONICS

A modified CCD fabrication process has been developed for producing an overlapping gate structure which permits submicron control of the gap size while using conventional optical lithography. This process has been used to fabricate a four-phase, 16-stage Schottky barrier CCD on GaAs with a charge transfer inefficiency of less than 2×10^{-4} at a 1-MHz clock rate, indicating that charge loss due to potential troughs between the gates has been essentially eliminated.

Improved performance has been observed on a high-speed GaAs p-i-n photodiode fabricated on a semi-insulating GaAs substrate. In addition to an impulse response of 19 ps FWHM to 4-ps laser pulses at 757 nm, it exhibits an external quantum efficiency of 15 percent at 757 and 814 nm. The diode design permits integration in monolithic optoelectronic circuits containing such devices as GaAs field-effect transistors.

Oscillations have been observed for the first time from double-barrier resonant tunneling structures. At sufficiently high current densities and proper impedance match to the resonant circuit, the devices oscillated readily in the negative resistance region. A maximum output power of $5 \mu\text{W}$ and oscillation frequency of 18 GHz, with a DC to RF efficiency of 2.4 percent at temperatures as high as 200 K have been obtained.

5. ANALOG DEVICE TECHNOLOGY

A new readout technique for a charge-coupled device (CCD) image processor has been demonstrated that provides, in a single, rapid readout operation, a histogram of the distribution of pixel intensities in the image. Examples of the use of such information are to provide rapid dynamic threshold levels for an image digitizer or, when applied to the difference of two images, to indicate when a change has occurred somewhere in a scene.

Using a SAW convolver as a continuously programmable matched filter for 92.5-MHz MSK-modulated PN waveforms, a technique has been demonstrated that provides a wideband receiver in a dense communication environment with the capability to suppress a strong signal from a nearby transmitter relative to weaker signals originating from more distant locations. A limiter followed by a bandpass filter will suppress the smaller signals by 6 dB relative to the larger constant-amplitude component. By subtracting this bandpass-limited reference signal from the original signal, the larger signal will be highly suppressed while the smaller signals are reduced by only 6 dB.

REPORTS ON SOLID STATE RESEARCH

1 August through 31 October 1984

PUBLISHED REPORTS

Journal Articles

JA No.

- | | | | |
|------|---|--|---|
| 5545 | Fabrication, Characterization, and Analysis of Mass-Transported GaInAsP/InP Buried-Heterostructure Lasers | Z.L. Liao
J.N. Walpole
D.Z. Tsang | IEEE J. Quantum Electron. QE-20, 855 (1984) |
| 5560 | Molecular Beam Epitaxy of GaAs and AlGaAs on Si | B-Y. Tsaur
G.M. Metzger | Appl. Phys. Lett. 45, 535 (1984), DTIC AD-A147400 |
| 5562 | Residual Donors in LEC Indium Phosphide | P.J. Dean*
M.S. Skolnick*
B. Cockayne*
W.R. MacEwan*
G.W. Iseler | J. Cryst. Growth 67, 486 (1984) |
| 5570 | Annealing of Damage in Se ⁺ -Implanted Indium Phosphide | J.D. Woodhouse
J.P. Donnelly
P.M. Nitishin
E.B. Owens
J.L. Ryan | Solid-State Electron. 27, 677 (1984), DTIC AD-A147972 |
| 5578 | Patterned Photonucleation of Chemical Vapor Deposition of Al by UV-Laser Photodeposition | J.Y. Tsao
D.J. Ehrlich | Appl. Phys. Lett. 45, 617 (1984), DTIC AD-A146896 |
| 5587 | Spectral Characteristics of (GaAl)As Diode Lasers at 1.7 K | J. Harrison
A. Mooradian | Appl. Phys. Lett. 45, 318 (1984), DTIC AD-A147193 |
| 5595 | Theoretical Analysis of Coherently Coupled Optical Waveguide Bends | L.M. Johnson
D. Yap | Appl. Opt. 23, 2988 (1984) |
| 5600 | Coupling Between Successive Ti:LiNbO ₃ Waveguide Bends and Branches | D. Yap
L.M. Johnson | Appl. Opt. 23, 2991 (1984), DTIC AD-A148146 |

* Author not at Lincoln Laboratory.

JA No.

- | | | | |
|------|--|--|---|
| 5601 | Q-Switching of Low-Threshold Buried-Heterostructure Diode Lasers at 10 GHz | D.Z. Tsang
J.N. Walpole
Z.L. Liao
S.H. Groves
V. Diadiuk | Appl. Phys. Lett. 45 , 204 (1984), DTIC AD-A147401 |
| 5607 | High Frequency Heterodyne Spectroscopy with Current-Modulated Diode Lasers | W. Lenth | IEEE J. Quantum Electron. QE-20 , 1045 (1984) |
| 5611 | Optimal Design of CdS- and Cd _{0.8} Zn _{0.2} S-Based Single-Junction and Multijunction Solar Cells | J.C.C. Fan
B.J. Palm | Solar Cells 12 , 401 (1984) |
| 5627 | Picosecond Gain Measurements in a GaAlAs Diode Laser | W. Lenth | Opt. Lett. 9 , 396 (1984), DTIC AD-A147993 |
| 5637 | Optical Guided-Wave Gallium Arsenide Monolithic Interferometer | J.P. Donnelly
N.L. DeMeo
G.A. Ferrante
K.B. Nichols
F.J. O'Donnell | Appl. Phys. Lett. 45 , 360 (1984), DTIC AD-A147251 |
| 5644 | Use of Spatial Time-Division Repetition Rate Multiplication of Mode-Locked Laser Pulses to Generate Microwave Radiation from Optoelectronic Switches | A. Mooradian | Appl. Phys. Lett. 45 , 494 (1984), DTIC AD-A147129 |
| 5653 | Comparison of Laser-Initiated and Thermal Chemical Vapor Deposition of Tungsten Films | T.F. Deutsch
D.D. Rathman | Appl. Phys. Lett. 45 , 623 (1984), DTIC AD-A147402 |

Meeting Speeches**MS No.**

- | | | | |
|------|--|------------------------------|--|
| 5264 | Recent Advances in Transition-Metal-Doped Tunable Lasers | P.F. Moulton
A. Mooradian | <i>Beijing/Shanghai Proceedings of an International Conference on Lasers, May 1980 (Wiley, England, 1983), pp. 437-446</i> |
|------|--|------------------------------|--|

MS No.

- | | | | |
|------|--|---|---|
| 6433 | Fabrication and Characterization of Ti-Indiffused and Proton Exchange Waveguides in LiNbO_3 | R.A. Becker | <i>Processing of Guided Wave Optoelectronic Materials</i> , Proc. SPIE 460, 95-100 (1984) |
| 6438 | An Electroabsorptive CCD Spatial Light Modulator | R.H. Kingston
B.E. Burke
K.B. Nichols
F.J. Leonberger | <i>Spatial Light Modulators and Applications</i> , Proc. SPIE 465, 9-11 (1984), DTIC AD-A147194 |
| 6444 | AlGaAs Shallow-Homojunction Solar Cells for Tandem Applications | R.P. Gale
G.W. Turner
J.C.C. Fan
R.L. Chapman
J.V. Pantano | Proc. Seventeenth IEEE Photovoltaic Specialists Conference, Kissimmee, Florida, 1-4 May 1984, pp. 721-725, DTIC AD-A147228 |
| 6450 | GaAs CLEFT Solar Cells for Space Applications | J.C.C. Fan
R.W. McClelland
B.D. King | Proc. Seventeenth IEEE Photovoltaic Specialists Conference, Kissimmee, Florida, 1-4 May 1984, pp. 31-35, DTIC AD-A147192 |
| 6452 | GaAsP Shallow-Homojunction Solar Cells for Tandem Applications | R.W. McClelland
B.D. King
J.C.C. Fan
R.L. Chapman | Proc. Seventeenth IEEE Photovoltaic Specialists Conference, Kissimmee, Florida, 1-4 May 1984, pp. 452-454, DTIC AD-A147321 |
| 6456 | GaAs/Ge/Si Solar Cells | B-Y. Tsaur
J.C.C. Fan
G.W. Turner
B.D. King
R.W. McClelland
G.M. Metze | Proc. Seventeenth IEEE Photovoltaic Specialists Conference, Kissimmee, Florida, 1-4 May 1984, pp. 440-444, DTIC AD-A147226 |
| 6465 | Masked Ion Beam Lithography Using Stencil Masks | J.N. Randall
D.C. Flanders
N.P. Economou | <i>Electron-Beam, X-Ray, and Ion-Beam Techniques for Submicrometer Lithographies III</i> , A. Wagner, Ed., Proc. SPIE 471, 47-52 (1984) |

MS No.

- | | | | |
|------|---|--|--|
| 6483 | Rapid Thermal Annealing of Composite TaSi ₂ /n ⁺ Poly-Si Silicide Films | D.L. Kwong*
R. Kwor*
B-Y. Tsaur
K. Daneshvar* | Proc. Materials Research Society 23, Elsevier, New York, 1984, pp. 733-738 |
| 6640 | Silicon Permeable Base Transistors | D.D. Rathman
B.A. Vojak
D.C. Flanders
N.P. Economou | Extended Abstracts of the Sixteenth (1984 International) Conference on Solid State Devices and Materials, Kobe, Japan, 1984, pp. 305-308 |
| 6651 | A New High-Efficiency GaAs Solar Cell Structure Using a Heterostructure Back-Surface Field | R.P. Gale
J.C.C. Fan
G.W. Turner
R.L. Chapman | Proc. Seventeenth IEEE Photovoltaic Specialists Conference, Kissimmee, Florida, 1-4 May 1984, pp. 1422-1425, DTIC AD-A147534 |

* * * * *

UNPUBLISHED REPORTS

Journal Articles

JA No.

- | | | | |
|------|---|--|--|
| 5610 | Submicrometer Patterning by Projected Excimer Laser Beam Induced Chemistry | D.J. Ehrlich
J.Y. Tsao
C.O. Bozler | Accepted by J. Vac. Sci. Technol. |
| 5613 | Experimental Tests of Open-Loop Maximum-Power-Point Tracking Techniques for Photovoltaic Arrays | G.W. Hart*
H.M. Branz
C.H. Cox | Accepted by Solar Cells |
| 5621 | A Review of Silicon-on-Insulator Technology for VLSI | B-Y. Tsaur | Accepted for Annual Report of the Chinese-American Academic and Professional Association |

* Author not at Lincoln Laboratory.

JA No.

- | | | | |
|------|--|---|--|
| 5623 | Advances in LEC Growth of InP Crystals | G.W. Iseler | Accepted by J. Electron. Mater. |
| 5635 | Traveling-Wave Electrooptic Modulator with Maximum Bandwidth-Length Product | R.A. Becker | Accepted by Appl. Phys. Lett. |
| 5648 | A High Frequency GaAs Optical Guided-Wave Electrooptic Interferometric Modulator | J.P. Donnelly
N.L. DeMeo
G.A. Ferrante
K.B. Nichols | Accepted by IEEE J. Quantum Electron. |
| 5651 | Detrimental Optical Properties of Germanium Intermediate Layers in Monolithic Tandem Solar Cell Structures | G.W. Turner | Accepted by Solar Cells |
| 5652 | Merged CMOS/Bipolar Technologies Utilizing Zone-Melting-Recrystallized SOI Films | B-Y. Tsaur
R.W. Mountain
C.K. Chen
J.C.C. Fan | Accepted by IEEE Electron Device Lett. |
| 5654 | Donor Identification in Liquid Phase Epitaxial Indium Phosphide | M.S. Skolnick*
P.J. Dean*
S.H. Groves
E. Kuphal* | Accepted by Appl. Phys. Lett. |
| 5656 | Metal-Semiconductor Field-Effect Transistors Fabricated in GaAs Layers Grown Directly on Si Substrates by Molecular Beam Epitaxy | G.M. Metz
H.K. Choi
B-Y. Tsaur | Accepted by Appl. Phys. Lett. |
| 5660 | Masked Ion Beam Resist Exposure using Grid Support Stencil Masks | J.N. Randall
D.C. Flanders
N.P. Economou
J.P. Donnelly
E.I. Bromley | Accepted by J. Vac. Sci. Technol. |
| 5665 | Error Reduction in Laser Remote Sensing: Combined Effects of Cross-Correlation and Signal Averaging | N. Menyuk
D.K. Killinger
C.R. Menyuk* | Accepted by Appl. Opt. |

* Author not at Lincoln Laboratory.

JA No.

- | | | | |
|------|--|--|--|
| 5671 | Selective Tungsten Silicide Formation by Ion Beam Mixing and Rapid Thermal Annealing | B-Y. Tsaur
C.K. Chen
C.H. Anderson, Jr. | Accepted by J. Appl. Phys. |
| 5676 | Quantum Well Oscillators | T.C.L.G. Sollner
P.E. Tannenwald
D.D. Peck
W.D. Goodhue | Accepted by Appl. Phys. Lett. |
| 5687 | High Resistivity InGaAs(Fe) Grown by an LPE Substrate-Transfer Technique | S.H. Groves
V. Diadiuk
M.C. Plonko
D.L. Hovey | Accepted by Appl. Phys. Lett. |
| 5688 | Lateral Photodetectors on Semi-Insulating InGaAs and InP | V. Diadiuk
S.H. Groves | Accepted by Appl. Phys. Lett. |
| 5691 | Microwave Operation of Submicrometer Channel-Length Silicon MOSFETs | D.C. Shaver | Accepted by IEEE Electron Device Lett. |

Meeting Speeches***MS No.**

- | | | | |
|-------|---|---------------|--|
| 6078D | Excitation of Surface Optical Waves and Material Ripples by Stimulated Scattering | S.R.J. Brueck | Seminar, University of Lund, Lund, Sweden, 21 September 1984 |
| 6078E | Excitation of Surface Optical Waves and Material Ripples by Stimulated Scattering | S.R.J. Brueck | } Seminar, Norwegian Defense Research Establishment, Oslo, Norway, 25 September 1984 |
| 6650A | Optical Microanalysis of Device Materials and Structures | S.R.J. Brueck | |
| 6400D | Laser Surface Modifications for Patterned Growth | D.J. Ehrlich | Dry Processing Symposium, Yorktown Heights, New York, 9 November 1984 |

* Titles of Meeting Speeches are listed for information only. No copies are available for distribution.

MS No.

6549	10.6- μ m Photomixer Arrays at 195 K	D.L. Spears	1984 Meeting of the IRIS Specialty Group on Infrared Detectors, Seattle, Washington, 14-16 August 1984
6550A	Tunable Solid-State Lasers	P.F. Moulton	NASA Workshop, Menlo Park, California, 1-3 October 1984
6562B	Mass-Transported Buried-Heterostructure Lasers and Integrated Mirrors	Z.L. Liao	Seminar GTE Sylvania, Waltham, Massachusetts, 9 October 1984
6596	Physics and Technology of Submillimeter Wave Detectors	T.C.L.G. Sollner P.E. Tannenwald	Ninth International Conference on IR and Millimeter Waves, Takarazuka, Japan, 23-26 October 1984
6605	Future of Cryogenic Devices for Signal Processing Applications	S.A. Reible	Advanced Signal Processing Workshop, University of Warwick, United Kingdom, 17-21 September 1984
6610A	Permeable Base Transistor with a Base Grating Overgrown by MBE and Its Microwave Characteristics	A.R. Calawa M.J. Manfra G.A. Lincoln	Third International Conference on MBE, San Francisco, California, 1-3 August 1984
6619	A New Quantum State in Multiple Quantum Well Structures	H.Q. Le* B. Lax B.A. Vojak A.R. Calawa W.D. Goodhue	Seventeenth International Conference on Physics of Semiconductors, San Francisco, California, 6-10 August 1984
6628A	The Permeable Base Transistor	C.O. Bozler	IBM Semiconductor Colloquium, Yorktown Heights, New York, 22 October 1984

* Author not at Lincoln Laboratory.

MS No.

6633	Novel Processing Using Self-Developed Resist and Masked Ion Beam Exposures	J.N. Randall M.W. Geis	} IEEE Workshop on Micrometer and Submicrometer Lithography, Hyannis, Massachusetts, 28-31 August 1984
6714A	Factors Influencing Damage in Dry Etching	S.W. Pang	
6642	Superconductive Convolver with Junction Ring Mixers	S.A. Reible	} 1984 Applied Superconductivity Conference, San Diego, California, 9-13 September 1984
6711	Superconductive Delay-Line Technology and Applications	R.S. Withers A.C. Anderson J.B. Green S.A. Reible	
6735	Signal Processing: Opportunities for Superconductive Circuits	R.W. Ralston	
6649	Efficient Solar Cells using Ultrathin III-V Films	J.C.C. Fan	
6654	Guided-Wave Optics in LiNbO ₃ : Physical Properties, Devices and Signal Processing Systems	R.A. Becker	} The Electrochemical Society, New Orleans, Louisiana, 7-12 October 1984
6661	Radiation Field Coupling in Optical Waveguide Structures with Closely Spaced Abrupt Bends and Branches	D. Yap L.M. Johnson	
6674	Monolithic Integration of GaAs and Si	J.C.C. Fan	} SPIE Symposium on Optical and Electrooptical Engineering, Cambridge, Massachusetts, 21-26 October 1984
6674A	Monolithic Integration of GaAs and Si	J.C.C. Fan	
			} 1984 International Conference on Solid State Devices and Materials, Kobe, Japan, 30 August — 1 September 1984
			} 1984 International Electronic Devices and Materials Symposium, Hsinchu, Taiwan, 4 September 1984

MS No.

6683	Mass-Transported GaInAsP/InP Buried-Heterostructure Lasers	Z.L. Liao D.C. Flanders J.N. Walpole D.Z. Tsang N.L. DeMeo	} Ninth IEEE International Semiconductor Laser Conference, Rio de Janeiro, Brazil, 7-10 August 1984
6685	Q-Switching of GaInAsP Diode Lasers up to 14.4 GHz	D.Z. Tsang J.N. Walpole Z.L. Liao S.H. Groves	
6687	Advances in Devices Fabricated in Zone-Melting-Recrystallized SOI Films	B-Y. Tsaur R.W. Mountain C.K. Chen J.C.C. Fan	1984 IEEE SOS, SOI Technology Workshop, Hilton Head Island, South Carolina, 2-4 October 1984
6692	Graphite-Strip-Heater Zone-Melting Recrystallization of Si Films	J.C.C. Fan	1984 Seoul International Symposium on the Physics of Semiconductors and Its Applications, Seoul, Korea, 27-28 August 1984
6697	Future Laser Systems for Atmospheric Applications: State of Development and Perspectives	D.K. Killinger A. Mooradian P.F. Moulton N. Menyuk	Twelfth International Laser Radar Conference, Aix-en-Provence, France, 13-17 August 1984
6697A	Laser Remote Sensing of the Atmosphere	D.K. Killinger	Optical Society of America, New England Chapter Meeting, Lexington, Massachusetts, 18 October 1984
6698	CCD Parallel Processing Architecture	A.M. Chiang	International Conference on Digital Signal Processing, Florence, Italy, 5-8 September 1984

MS No.

6717	Laser-Microchemical Processing	D.J. Ehrlich	} International Dry Processing Symposium, Tokyo, Japan, 11-12 October 1984
6743	Ion Beam Induced Etching	M.W. Geis J.N. Randall N.N. Efremow G.A. Lincoln S.W. Pang N.P. Economou	
6723	Laser Microchemical Techniques for Electronics	D.J. Ehrlich	Workshop on Applications of Free Electron Lasers, Castel Gandolfo, Italy, 10-12 September 1984
6724	Pitfalls of Dry Etching	S.W. Pang	SEMICON East, Boston, Massachusetts, 18-20 September 1984
6728	LiNbO ₃ and GaAs Guided-Wave Signal Processing Devices	F.J. Leonberger R.A. Becker L.M. Johnson J.P. Donnelly R.H. Kingston	Conference on Integrated Optical and Related Technologies for Signal Processing, Florence, Italy, 10-11 September 1984
6732	Optical Techniques for Processing of Electrical Signals	R.C. Williamson	Seminar, IEEE Quantum Electronics and Applications, Boston Chapter, Waltham, Massachusetts, 13 September 1984
6732A	Optical Techniques for Processing of Electrical Signals	R.C. Williamson	Seminar, Raytheon Research Laboratories, Lexington, Massachusetts, 17 October 1984
6744	Resist Sensitivity Enhancement in Microlithography by In-Situ Polymerization	J.A. Moore* J.C. Corelli* A.J. Steckl* J.T. Warden* R. Tarro* J.N. Randall	American Chemical Society, Philadelphia, Pennsylvania, 26-31 August 1984
6761	Electron-Beam Techniques for Wafer-Scale Fabrication	D.C. Shaver	Honeywell Microelectronics Conference, Minneapolis, Minnesota, 12 September 1984

* Author not at Lincoln Laboratory.

ORGANIZATION

SOLID STATE DIVISION

A.L. McWhorter, *Head*
I. Melngailis, *Associate Head*
E. Stern, *Associate Head*
J.F. Goodwin, *Assistant*

P.E. Tannenwald, *Senior Staff*

QUANTUM ELECTRONICS

A. Mooradian, *Leader*
P.L. Kelley, *Associate Leader*

Barch, W.E.	Harrison, J.*
Belanger, L.J.	Johnson, B.C.*
Brueck, S.R.J.	Killinger, D.K.
Burke, J.W.	Menyuk, N.
Bushee, J.F., Jr.	Moulton, P.F.
DeFeo, W.E.	Sedlacek, J.H.C.
Ehrlich, D.J.	Sharpe, K.A.
Feldman, B.	Sullivan, D.J.
Hancock, R.C.	

ELECTRONIC MATERIALS

A.J. Strauss, *Leader*
J.C.C. Fan, *Associate Leader*
H.J. Zeiger, *Senior Staff*

Anderson, C.H., Jr.	Kolesar, D.F.
Button, M.J.	Krohn, L., Jr.
Chapman, R.L.	Mastromattei, E.L.
Chen, C.K.	McClelland, R.W.
Choi, H.K.	Metze, G.M.
Connors, M.K.	Nitishin, P.M.
Delaney, E.J.	Pantano, J.V.
Fahey, R.E.	Tracy, D.M.
Finn, M.C.	Tsaur, B-Y.
Gale, R.P.	Turner, G.W.
Iseler, G.W.	Windhorn, T.H.
King, B.D.	

APPLIED PHYSICS

R.C. Williamson, *Leader*
D.L. Spears, *Assistant Leader*
T.C. Harman, *Senior Staff*
R.H. Rediker, *Senior Staff*

Becker, R.A.
Cox, C.H., III
DeMeo, N.L., Jr.
Diadiuk, V.
Donnelly, J.P.
Duffy, P.E.†
Ferrante, G.A.
Groves, S.H.

Hovey, D.L.
Johnson, L.M.
Liau, Z.L.
Lind, T.A.
McBride, W.F.
Molter-Orr, L.*
O'Donnell, F.J.
Plonko, M.C.

Reeder, R.E.
Schloss, R.P.*
Tsang, D.Z.
Walpole, J.N.
Whitaker, N.*
Woodhouse, J.D.
Yap, D.*

* Research Assistant

† Part Time

ANALOG DEVICE TECHNOLOGY

R.W. Ralston, *Leader*

R.S. Withers, *Assistant Leader*

Anderson, A.C.
Arsenault, D.R.
Boisvert, R.R.
Bouman, C.A.
Brogan, W.T.
Delaney, M.*
Dolat, V.S.
Fischer, J.H.

Fitch, G.L.
Flynn, G.T.
Green, J.B.
Hauser, E.M.
Holtham, J.H.
Kernan, W.C.
Lattes, A.L.
Macedo, E.M., Jr.

Macropoulos, W.
Marden, J.A.
Melngailis, J.†
Oates, D.E.
Sage, J.P.
Smith, L.N.
Yao, I.

MICROELECTRONICS

W.T. Lindley, *Leader*

N.P. Economou, *Associate Leader*

B.B. Kosicki, *Assistant Leader*

R.A. Murphy, *Assistant Leader*

Astolfi, D.K.
Bozler, C.O.
Bromley, E.I.
Burke, B.E.
Calawa, A.R.
Chen, C.L.
Chiang, A.M.
Clifton, B.J.
Correa, C.A.
Daniels, P.J.
Durant, G.L.
Efremow, N.N., Jr.
Felton, B.J.
Geis, M.W.

Goodhue, W.D.
Gray, R.V.
Hollis, M.A.
Lax, B.†
LeCoz, Y.L.*
Lincoln, G.A., Jr.
Lyszcza, T.M.
Mahoney, L.J.
Manfra, M.J.
McGonagle, W.H.
Mroczkowski, I.H.
Mountain, R.W.
Nichols, K.B.
Pang, S.W.

Parker, C.D.
Piacentini, W.J.
Pichler, H.H.
Rabe, S.
Randall, J.N.
Rathman, D.D.
Shaver, D.C.
Silversmith, D.J.
Smythe, D.L., Jr.
Sollner, T.C.L.G.
Taylor, J.A.*
Vera, A.
Wilde, R.E.

* Research Assistant

† Part Time

1. SOLID STATE DEVICE RESEARCH

1.1 LATERAL PHOTODETECTORS ON SEMI-INSULATING InGaAs AND InP

Interest continues in developing sensitive, high-speed photodetectors operating in the 1.0- to 1.5- μm region of the spectrum. For many applications it is desirable to have structures that can be easily integrated with other electronic components. Here, we describe a new kind of PIN-like photodetector which satisfies the above performance and fabrication requirements. This device has high quantum efficiency, a very fast response time, and is fabricated simply by evaporating and alloying n- and p-type contact metals on semi-insulating material. The very low carrier concentration (approximately intrinsic) of the material plays a key role, and to emphasize this we refer to these devices as PSIN (p-semi-insulating-n) photodetectors.

Devices on both semi-insulating InP and InGaAs were fabricated and tested. Both materials have low surface recombination velocities, which is essential for high quantum efficiency. InP PSIN devices were made on Fe-doped LEC-grown bulk InP with very low carrier concentrations ($n \approx 7 \times 10^7 \text{ cm}^{-3}$) and very high resistivity ($\rho \approx 3 \times 10^7 \Omega\text{-cm}$). $\text{In}_{0.53}\text{Ga}_{0.47}\text{As}$ PSIN devices were fabricated on Fe-doped LPE material grown on InP:Fe substrates.^{1,2} The epitaxial layers were 2 to 4 μm thick with $n \approx 1 \times 10^{12} \text{ cm}^{-3}$ and $\rho \approx 2500 \Omega\text{-cm}$, which are also intrinsic values consistent with the narrower bandgap of InGaAs.

A cross section of the InGaAs PSIN device structure is shown in Figure 1-1(a). Except for the absence of the LPE-grown InGaAs:Fe layer, the InP device structure is identical. The stippled areas indicate the p- and n-regions formed by diffusion of the dopants from the contact metals into the semiconductor; the i-region is formed by the semi-insulating material itself. The devices consisted of 100- μm -wide electrodes with gap spacings of 3, 5, 10, and 20 μm . Contact metals were e-beam evaporated NiGeAu for the n-type, and ZnAu for the p-type electrodes. To insure effective alloying (without which the desired diode-like characteristics were not obtained), contact resistances were monitored by simultaneous fabrication of n-n and p-p contacts on n- and p-type substrates, yielding 5 and 9 Ω , respectively. Chips containing four devices, one of each gap size, were mounted in high-frequency packages, with a single device ribbon-bonded to 50- Ω alumina microstrips.

Typical I-V characteristics of an InGaAs:Fe PSIN device in the dark and illuminated by an InGaAsP laser are shown in Figure 1-1(b). These curves clearly exhibit both diode-like rectification and photoresponse. Under reverse bias, low values of dark current ($<1 \text{ nA}$ at 10 V) and high breakdown voltage (50 V) are observed. The quantum efficiency was measured using a calibrated Ge photodetector and yielded a value of 40 percent at 20 V for 20- μm -gap devices without antireflection coating.

Device capacitance (C) values were obtained by measuring high-frequency insertion loss as a function of frequency by means of a spectrum analyzer and an RF generator.³ In the 50-MHz to 1-GHz range, $C \approx 50 \text{ fF}$ was calculated for 3- μm -gap devices. The capacitance

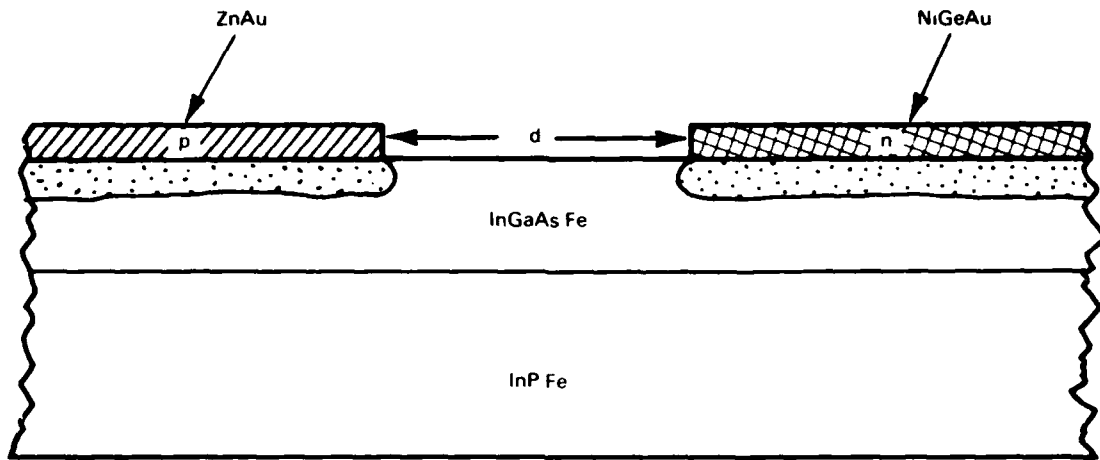


Figure 1-1(a). Schematic cross section of InGaAs PSIN structure. Gap spacing (d) is 3, 5, 10, or 20 μm .

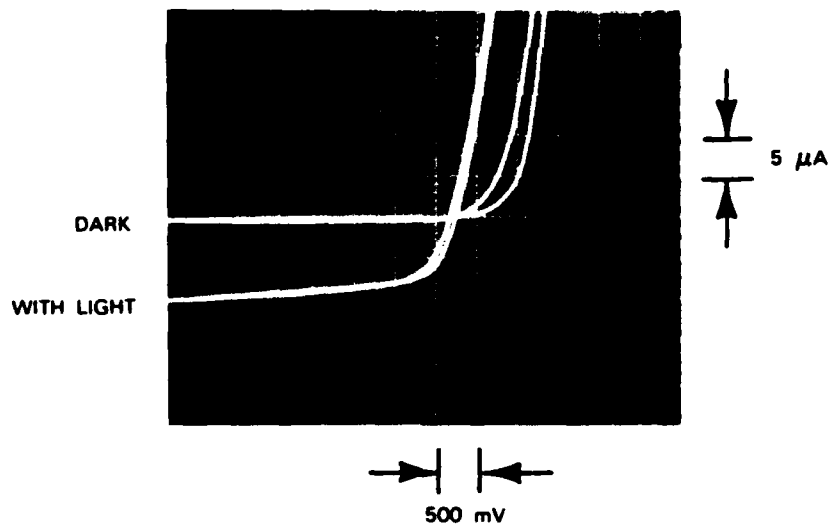


Figure 1-1(b). Curve tracer I-V characteristics of a 20- μm PSIN device in dark and under illumination.

142702-N-02

146311-R-01

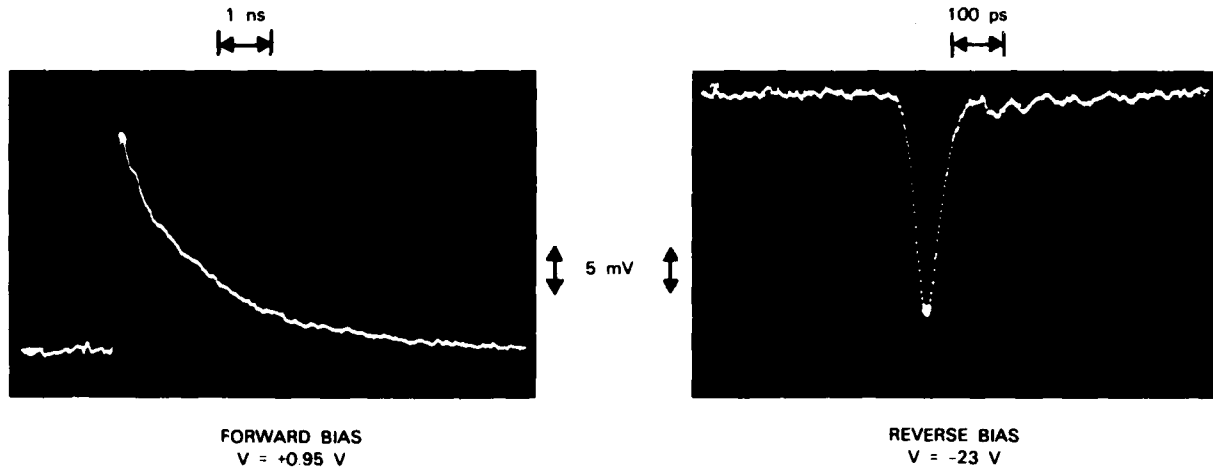


Figure 1-2. Pulse response of a 3- μm PSIN device, under forward and reverse bias, to a comb-generator-driven InGaAsP laser ($\lambda = 1.24 \mu\text{m}$). Notice different time scales but similar peak heights. FWHM is 1.2 ns and 57.2 ps under forward and reverse bias, respectively.

decreased linearly with $1/d$ (the reciprocal of the gap size), and by extrapolating the data to zero, a value for the parasitic capacitance of ≈ 18 fF was obtained. In contrast to conventional photodiodes with comparable-size active areas, even small-gap PSIN detectors are not RC-limited. The PSIN device capacitance was independent of reverse bias, indicating that the gap region is depleted at $V = 0$, as expected. Response times of the PSIN devices were measured using 100-MHz comb-generator-driven GaAs or InGaAsP diode lasers, with the output of the photodetector being monitored directly on a sampling oscilloscope. Typical response times under forward and reverse bias are shown in Figure 1-2 for a 3- μm -gap InGaAs:Fe device. The forward-bias pulse full-width-at-half-maximum (FWHM) is of the order of a nanosecond and corresponds to the carrier lifetime in InGaAs:Fe; this fact is confirmed by the similar values of FWHM obtained when two n contacts from adjacent PSIN devices are bonded to the package in a typical photoconductive configuration. Under reverse bias, where the carriers are swept out before they can recombine, $\text{FWHM} \approx 60$ ps. The transition from forward to reverse bias is smooth, with the forward FWHM decreasing with decreasing bias. The photocurrent actually goes to zero at +0.3 V; at $V = 0$, there is a small negative current pulse whose FWHM is already 100 ps. At a few volts reverse bias, FWHM becomes independent of voltage. The FWHM for the 3-, 5-, 10-, and 20- μm -gap devices are 50, 50, 60, and 90 ps, respectively. Comparison of these measured values with calculated transit times indicates that the 10- and 20- μm devices are transit time limited, whereas the 3- and 5- μm devices are limited by the measurement system response time. As expected, in no case was the device response time RC-limited.

Thus, because of their simple fabrication process, planar configuration, and performance characteristics, PSIN detectors are attractive for applications in optical communications and optical signal processing.

V. Diadiuk
S.H. Groves

1.2 POWER SPLITTING BEHAVIOR OF OPTICAL WAVEGUIDE STRUCTURES WITH CLOSELY SPACED ABRUPT BENDS AND BRANCHES

Optical waveguide structures containing successive bends and branches are useful for distributing optical power in multi-device integrated optical circuits. Space limitations may require that the bends and branches in complex structures be spaced closely together. We have recently performed the first experimental and theoretical study of structures with closely spaced bends and branches.⁴ Radiation-field coupling between the bends and branches can significantly affect the behavior of these structures.

Single-mode Ti:LiNbO₃ channel-waveguide structures consisting of a symmetric Y-branch preceded by an abrupt bend were fabricated and tested. The waveguides were made by diffusing 4- μm -wide, 400- \AA -thick titanium strips into X-cut lithium niobate substrates at 1000°C for 5-3/4 hours. These guides are single mode at 0.83 μm for both polarizations.

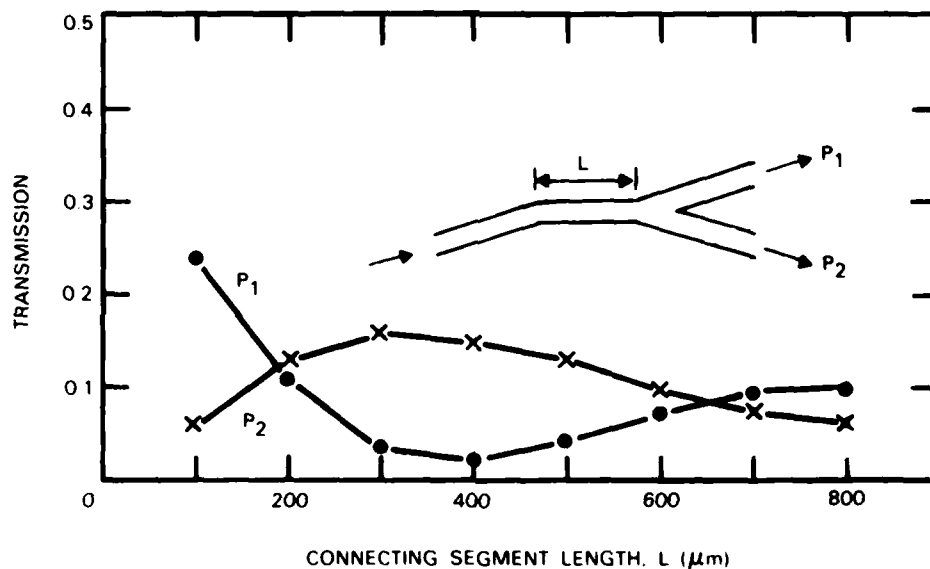


Figure 1-3. Measured transmission from two branch arms of bend-branch structures plotted vs their connecting-segment lengths. Measurements were made using TM-polarized light at a wavelength of 0.83 μm .

The measured TM transmission of a structure containing a 1° abrupt bend and a branch with a 1° half-angle is plotted in Figure 1-3. This structure was designed to enhance the bend-branch coupling effects rather than to minimize the losses. Note that the branch-arm transmission exhibits a strong oscillatory dependence on the length of the waveguide segment connecting the bend and the branch for lengths between 100 and 800 μm . The ratio of the two branch-arm transmissions ranges from 0 to ± 6 dB, with the oscillatory variation becoming less pronounced at longer connecting-segment lengths.

We have analyzed this structure and have shown that the transmission depends on both the interference between the guided and radiation modes propagating in the connecting segment and the change in the relative phases of the two local-normal modes propagating in the branch. We have also observed and analyzed the effect of the optical polarization and wavelength and the waveguide fabrication conditions. Conditions which result in a greater guided-mode effective index relative to the substrate index yield transmission vs connecting-segment length oscillations having shorter periods, and also enhance the effect of propagation in the branch.^{4,5} Results of this study can be used to design compact single-mode multiple-branching circuits.

D. Yap
L.M. Johnson

1.3 INTEGRATED OPTICS WAVEFRONT MEASUREMENT SENSOR

The performance of the components for the wavefront measurement sensor shown in Figure 1-4 is being evaluated. In previous Solid State Research reports,^{6,7} we described the performance of the LiNbO_3 interferometers and horn antennas shown in Figure 1-4. The horn antennas increase the collection efficiency of incident radiation.⁷ Here, we report the performance of the interferometer array when its output is coupled into and then read out of a CCD imager. For equal power P incident on each of the waveguides, the output of

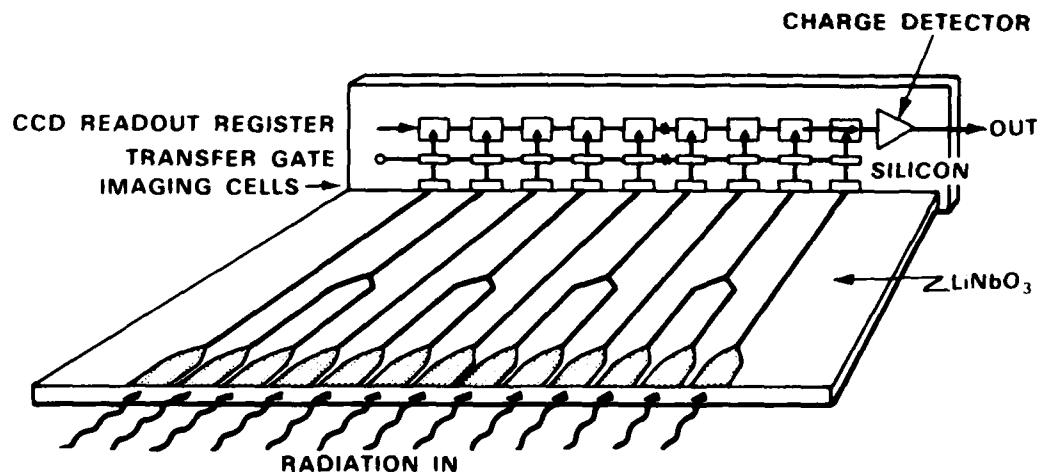


Figure 1-4. Wavefront measurement sensor consisting of an array of interferometers with horn antennas as input and CCD imager as output.

148310-N

the interferometer as a function of the phase difference ϕ between the optical waves incident on the two arms of the interferometer is given by

$$P_{\phi} = \left[2P \cos^2 \left(\frac{\phi - \phi_0}{2} \right) \right] B$$

where B takes into account additional losses in the interferometer arms (such as loss due to bends), and ϕ_0 is the built-in phase bias due to differences in interferometer arm lengths. The quantity ϕ_0 can be eliminated electrooptically or by real-time data processing. Typically, the variation in interferometer arm lengths is ± 20 nm in 1 cm (2 parts in 10^6), which corresponds for the GaAlAs laser radiation used ($\lambda = 370$ nm in LiNbO_3) to values of $\phi_0 \approx \pm 20^\circ$.

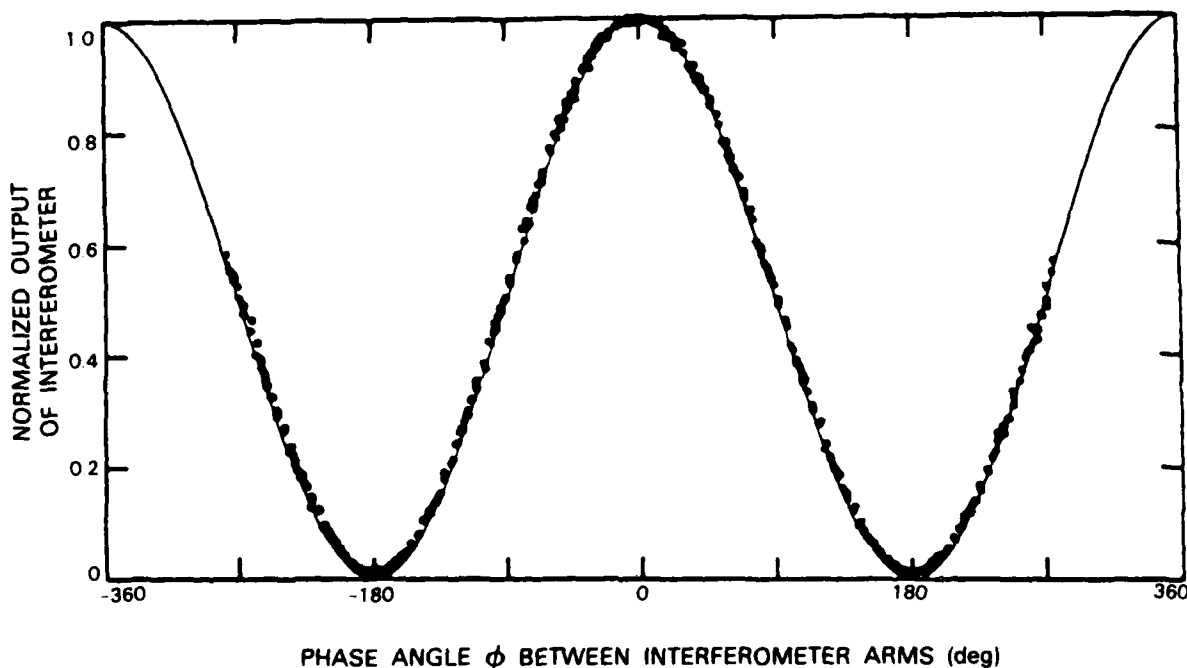


Figure 1-5. Experimental results P_{ϕ}/P for an array of 20 interferometers read out from a CCD imager are compared with theoretical curve $\cos^2(\phi/2)$. The more than 500 data points were normalized so maximum value of ratio for each interferometer was unity. Phase angle ϕ for experimental points for each interferometer was adjusted by a constant for each interferometer for best fit. Input radiation was at 810 nm.

Results of the evaluation of an array of interferometers read out by a CCD imager are shown in Figure 1-5. The agreement between experiment and theory is excellent. However, the experimental data do not go completely to zero at 180° phase angle because of a small amount of crosstalk between adjacent CCDs. This crosstalk is expected because the CCD imager used was designed for detection of the visible radiation, and the infrared GaAs laser

radiation ($\lambda = 810$ nm in air) produces electron-hole pairs deeper in the silicon than radiation at the design wavelength. Some of the charge produced deep in the silicon by the output of the straight (intensity monitoring) waveguides diffuses to adjacent CCD elements aligned with the interferometer (wavefront phase sensing) waveguides.

R.H. Rediker
T.A. Lind
B.E. Burke

1.4 A NOVEL GaInAsP/InP DISTRIBUTED FEEDBACK LASER

In recent years considerable effort has been devoted to the development of GaInAsP/InP distributed feedback (DFB) lasers for use as stable single-frequency sources in fiber optic communications.⁸⁻¹³ In this work we describe a novel device design which offers high performance and considerable fabrication simplicity.

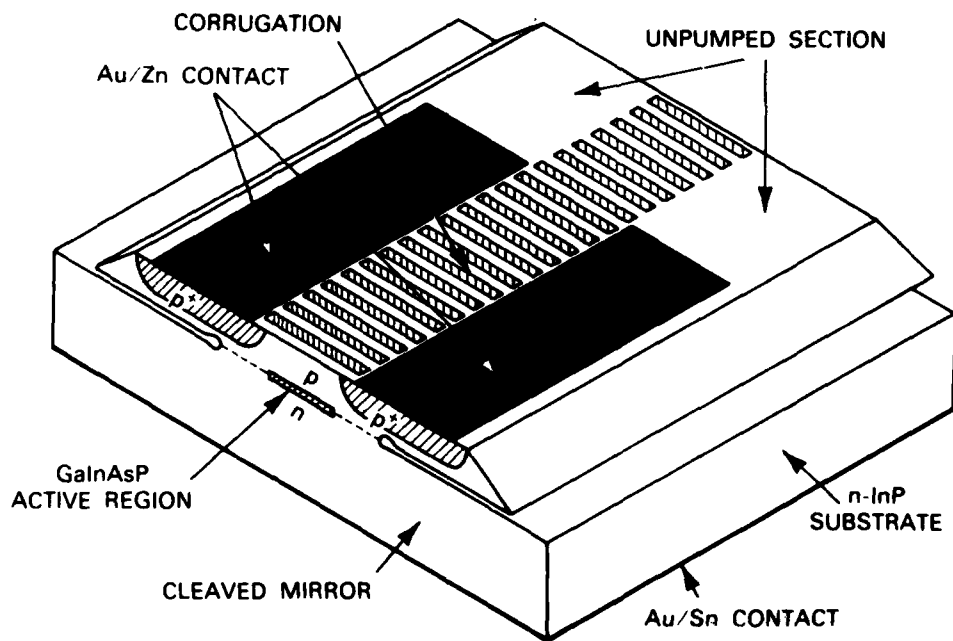


Figure 1-6. A schematic drawing of the GaInAsP/InP distributed feedback laser.

As illustrated in Figure 1-6, the device consists of a mass-transported buried heterostructure^{14,15} with a thin p-InP cap layer and a wide mesa on which a grating corrugation is etched in the middle, with Au/Zn alloyed contacts formed on each side. Sufficient coupling between the guided mode and the grating corrugation occurs if the InP cap layer is approximately $1 \mu\text{m}$ thick. The first-order grating corrugation with a periodicity of 2028 \AA and tooth height of approximately 2500 \AA is formed by using contact x-ray lithography¹⁶ (with a holographically generated mask pattern) and ion-beam-assisted etching using chlorine gas.¹⁷

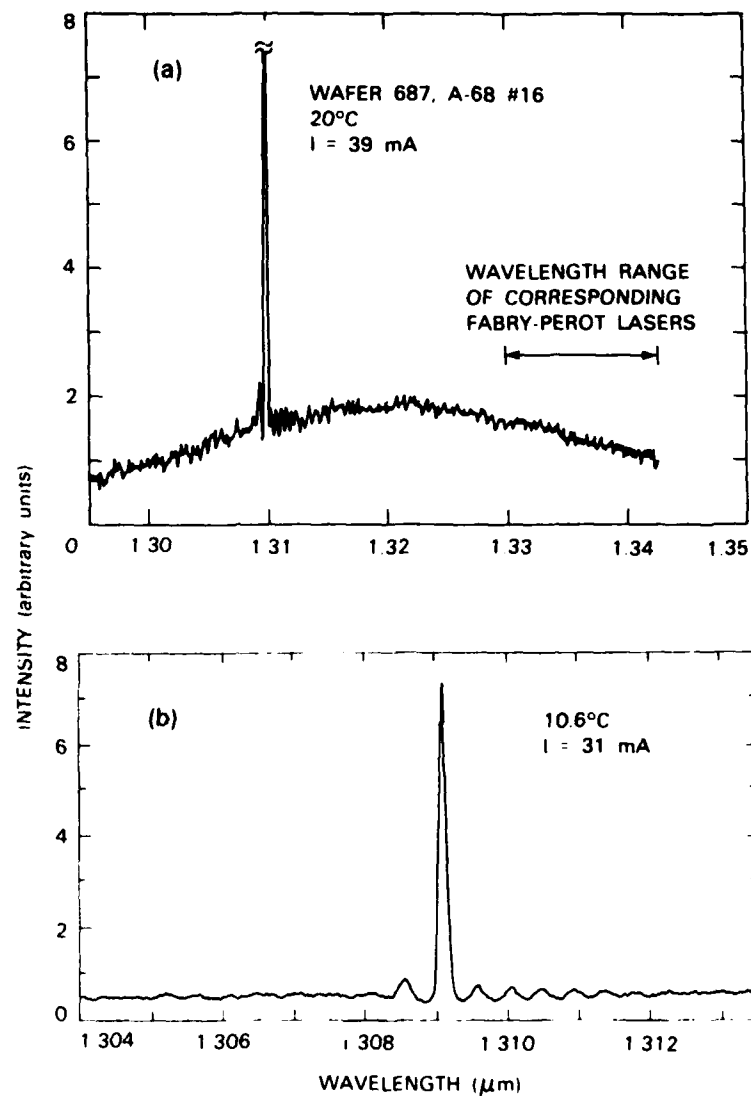


Figure 1-7. Emission spectra of one device just above lasing threshold at (a) 20°C and (b) 10.6°C. In (a), lasing modes are shown located on shorter-wavelength side of apparent spontaneous emission spectrum. Expanded wavelength scale in (b) shows more details of lasing spectrum.

149311-N

The wafer is then coated with a phosphosilicate glass (PSG) layer $0.4 \mu\text{m}$ thick (not shown in Figure 1-6), and a pair of stripe openings are defined in the PSG on top of the laser mesa for Au/Zn alloyed contacts. The rest of the metallization and dicing procedures are similar to those described previously.¹⁴ Each finished device has a cleaved front facet where the output power is measured; the rear is either cleaved or saw-cut.

Devices fabricated with a relatively long cavity (546 and $241 \mu\text{m}$ for pumped and unpumped sections, respectively) and saw-cut end show room-temperature pulsed threshold currents as low as 16 mA. Figure 1-7(a-b) shows CW emission spectra of a device just above its lasing threshold. As evident in Figure 1-7(a), the dominant lasing mode with a wavelength of $1.3098 \mu\text{m}$ is located on the shorter-wavelength side of the apparent spontaneous emission spectrum. This is a strong indication that the device is lasing in a DFB mode, since the Fabry-Perot modes should be located on the other side of the spontaneous spectrum where the gain maximum occurs. Indeed, Fabry-Perot mode operation at wavelengths of 1.33 to $1.34 \mu\text{m}$ was observed in shorter devices cleaved from the same wafer but without the unpumped section and saw-cut end. (Since the present DFB resonance wavelength is approximately 260 \AA away from the gain maximum, the Fabry-Perot mode can have a lower threshold current in devices without the unpumped section and saw-cut end.) Figure 1-7(b) shows a similar spectrum at 10.6°C and on different scales. Note that the threshold current drops to 31 mA. The series of peaks are likely the DFB modes, with the dominant one just outside the stop band.^{8,9}

At higher currents the dominant mode continues to grow, and the other DFB modes are at -37 dB when the current is 60 mA (which is approximately 1.54 times the threshold current I_{th}), as shown in Figure 1-8. However, a pair of modes of unknown origin with a -32-dB intensity are observed at $\pm 50 \text{ \AA}$ of the dominant DFB mode, as evident in Figure 1-8.

Shorter devices with smaller unpumped sections and both ends cleaved show room-temperature CW threshold currents as low as 13.5 mA but with more complicated mode behaviors. A device with pumped and unpumped sections of 318 and $152 \mu\text{m}$, respectively, showed a CW threshold current of 16 mA at room temperature and single-frequency operation (with sidemodes estimated at -30 dB) up to at least $2.5 I_{\text{th}}$ (with an output power of 2.8 mW), but with a mode hop from $\lambda = 1.3054$ to $1.3092 \mu\text{m}$ at $1.6 I_{\text{th}}$. Other devices with little or no unpumped sections lase in Fabry-Perot modes in the spectral region of 1.33 to $1.34 \mu\text{m}$, but still show considerably better mode purity than similar devices fabricated without the grating. (The latter also lase at wavelengths of 1.33 to $1.34 \mu\text{m}$.)

It is worth noting that the present device is considerably simpler than more conventional DFB lasers⁸⁻¹³ in terms of the waveguide and current-confinement structures and fabrication procedures. In particular, the grating is fabricated after the wafer growth is completed. This not only avoids the problems associated with growth over the grating,^{18,19} but also allows the wafer to be more thoroughly characterized before the grating is fabricated.

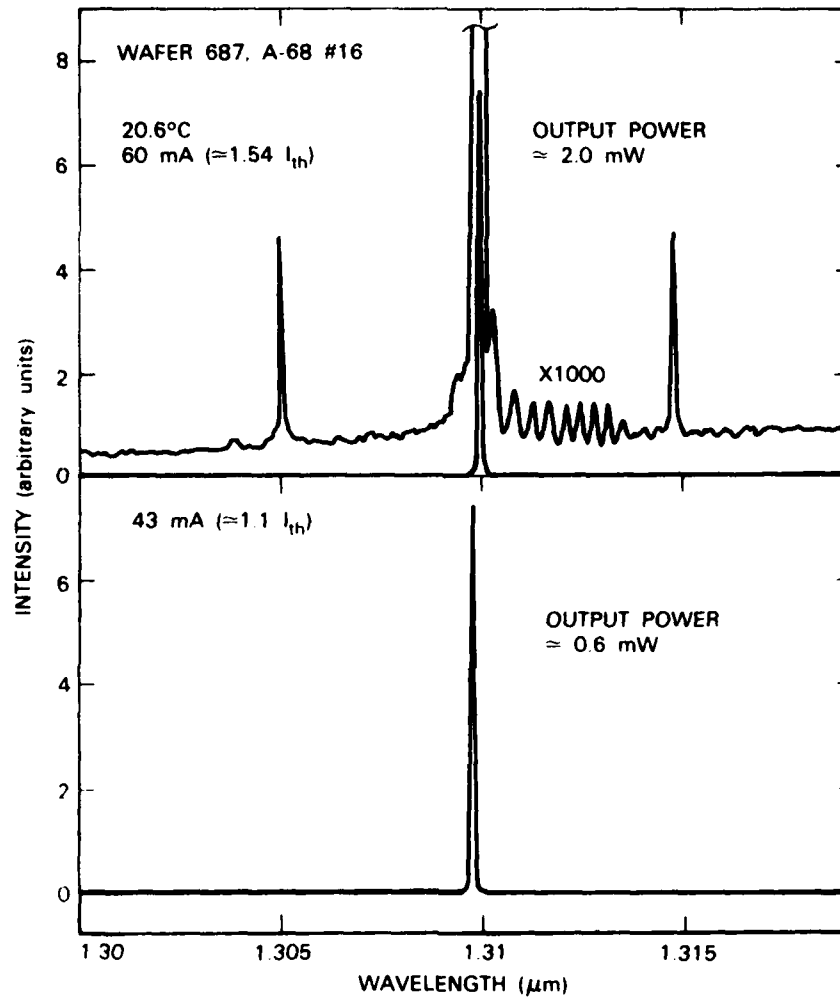


Figure 1-8. Emission spectra of device at 20.6°C and two different currents above threshold. Note that, at $I = 1.54 I_{th}$, sidemodes are lower than -32 dB.

144045-N-01

$\rho = 1 \times 10^{18} \text{ cm}^{-3}$
 PUMPED SECTION = $300 \mu\text{m}$
 CURRENT = 50 mA

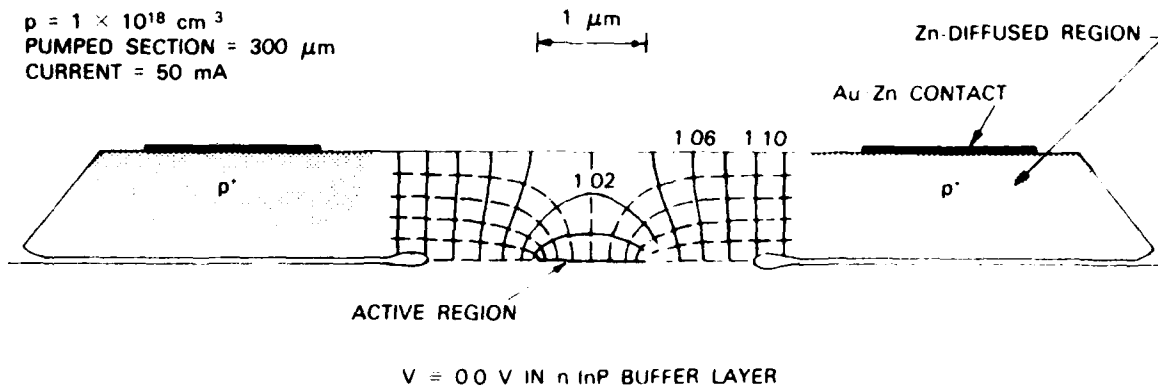


Figure 1-9. Calculated current and voltage distributions near active region in present structure. Dashed curves are streamlines of current flowing into active region. Solid curves are equipotentials, with numbers labeling voltage values in volts.

One potential problem of the present device is a possible leakage current I_H flowing through the InP pn homojunctions in the transported regions.¹⁵ (The homojunctions are illustrated as dashed-line segments in Figure 1-6.) This current leakage has been analyzed previously for other mass-transported buried-heterostructure lasers and has been shown to be capable of causing a saturation of light output at high current.¹⁵ A similar analysis has been carried out for the present structure,²⁰ in which the current I_Q flowing from the Au Zn contacts to the quaternary active region and the corresponding voltage distribution are modeled by using a conformal mapping technique, as illustrated in Figure 1-9. This analysis yields the forward-bias voltage along the homojunctions, which can in turn be used to estimate I_H . For small values of I_Q the calculated I_H is negligible, but its importance grows with increasing I_Q . The value of I_Q when $I_H = 0.1 I_Q$ is designated as I_1 and has been calculated for various device parameters; e.g., $I_1 = 74 \text{ mA}$ is obtained for the device of Figure 1-9. I_1 can be increased considerably by using a higher p-doping, narrower transported regions, a closer alignment of the Zn-diffused p^+ regions to the quaternary, or a larger pumped-section length. It is worth noting that, if the device were fabricated with an n-type mesa on a p-type substrate, there would be negligible voltage buildup due to high conductivity of n-type InP. However, the p-doping on the substrate side would need optimization in order to enable very high current operation.

In conclusion, a GaInAsP InP DFB laser has been realized in a simple new design in which the grating is fabricated on top of a mass-transported buried heterostructure. Threshold currents as low as 16 mA have been obtained, and still lower threshold current can possibly be achieved when the DFB resonance wavelength and the gain maximum are better matched. Further optimization of the doping scheme, the transported region width, and ohmic contact alignment is needed for high-power capability.

Z.L. Liao N.L. DeMeo
 D.C. Flanders D.K. Astolfi
 J.N. Walpole

1.5 SINGLE-MODE InP OPTICAL WAVEGUIDE CAPABLE OF PHASE MODULATION

Single-mode optical waveguides in which the effective index can be modulated via the electrooptic effect are necessary components of integrated-optic switches and modulators. In this section an InP single-mode p^+n-n^+ slab-coupled rib waveguide capable of phase modulating TE-polarized $1.3\text{-}\mu\text{m}$ radiation is described. It should be possible to fabricate two-guide coupler switches^{21,22} and interferometric modulators^{23,24} in InP using guides of this type.

A schematic cross section of a single-mode p^+n-n^+ InP slab-coupled rib waveguide is shown in Figure 1-10. The InP wafer used to fabricate these waveguides consisted of a (100)-oriented n^+ -substrate and a $5.5\text{-}\mu\text{m}$ -thick n -type layer with a carrier concentration of $\approx 2 \times 10^{16} \text{ cm}^{-3}$ grown by liquid phase epitaxy. To form the p^+ ribs, the wafer was implanted with a multi-energy Be-implanted schedule and annealed at 750°C , which produced a $1.5\text{-}\mu\text{m}$ -deep p^+ layer with a uniform carrier concentration of $\approx 2 \times 10^{18} \text{ cm}^{-3}$ (Reference 25). Rib waveguides approximately $5 \mu\text{m}$ wide were then formed by etching through the p^+ implanted layer into the epitaxial layer to a total depth of about $2 \mu\text{m}$. The waveguides were oriented for propagation along a (011) direction. A SiO_2 layer was deposited on

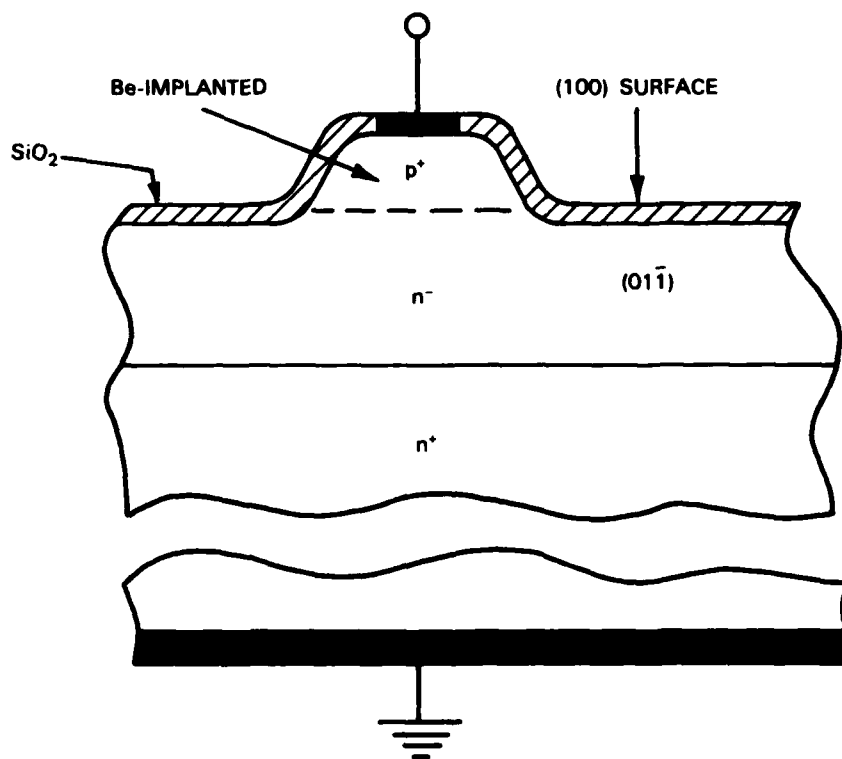


Figure 1-10. Schematic of single-mode p^+n-n^+ InP slab-coupled rib waveguide.

top of the wafer and Au/Mg and Au/Sn ohmic contacts were applied to the p^+ ribs and the back of the n^+ substrate, respectively. The input and output faces of the waveguide were then cleaved. These p^+-n-n^+ InP waveguides are similar to the GaAs waveguides recently used in a high-frequency interferometer.^{23,24} While the propagation loss of these guides was not measured in detail, a comparison of their transmitted power with that of guides of similar dimensions with known loss coefficients indicates that the loss per unit length is of the order of 1.5 to 2.0 cm^{-1} at 1.3 μm .

To determine the modulation characteristics of these waveguides, radiation from a single-mode GaInAsP/InP double-heterojunction laser operating at 1.3 μm was passed through a polarizer and end-fired coupled into the cleaved end face of one of the waveguides. The input radiation was polarized (nominally at 45° to the perpendicular) so that approximately an equal amount of TE- and TM-like radiation was excited in the guide. The output of the waveguide was passed through an analyzer and focused on a Ge photodiode.

Figure 1-11 shows the relative outputs of a 5-mm-long waveguide vs reverse bias on the p^+-n junction with the analyzer either parallel or perpendicular to the input polarization. Both curves approximate an offset cosine function of applied voltage. The maximum output with the analyzer parallel to the input polarization (minimum output with the analyzer perpendicular to the input polarization) does not occur at zero bias, because at low fields the

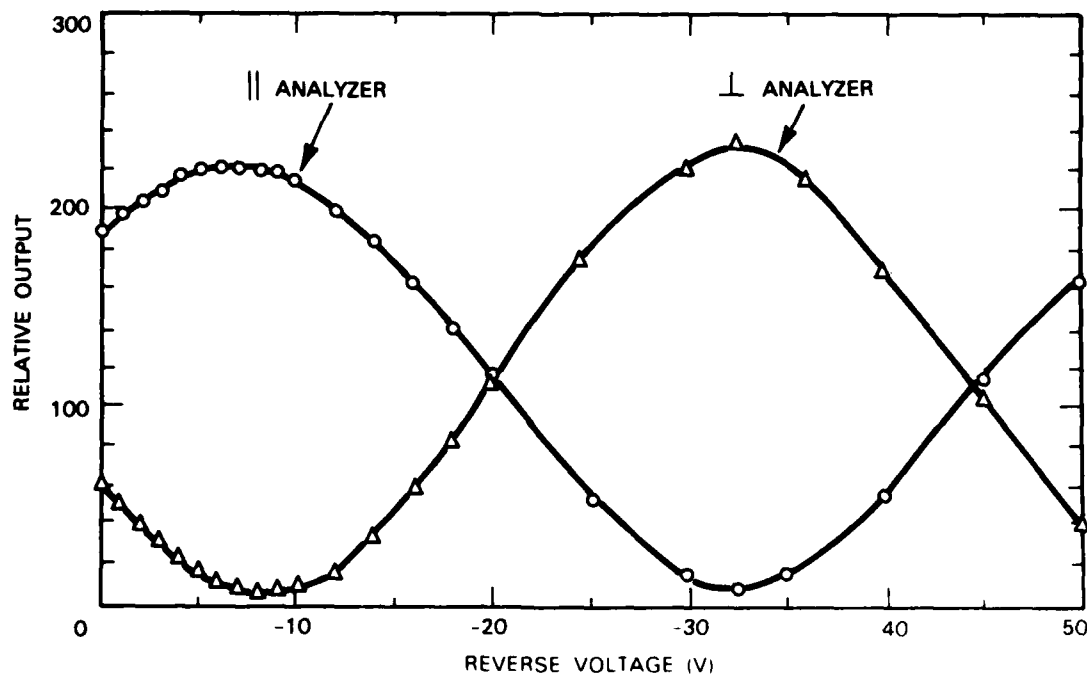


Figure 1-11. Relative output vs reverse bias of 5-mm-long p^+-n-n^+ InP slab-coupled rib waveguide with approximately equal amounts of TE- and TM-like radiation excited at input and an output analyzer parallel and perpendicular to input polarization.

velocity of the TE-like mode is slightly slower than that of the TM-like mode. Reverse biasing the p⁺-n junction decreases the refractive index in the plane of the junction [i.e., the (011) direction], but leaves the index perpendicular to the plane of the junction [i.e., the (100) direction] unaffected.^{26,27} Therefore, the velocity of the TE-like mode increases with reverse bias, while that of the TM-like mode is, at least to first order, not affected. This results in a change in phase of the TE-like mode relative to that of the TM-like mode at the output face, and produces the observed variation in relative output. The extinction ratio is about 16.5 dB. This relatively low value was obtained primarily because the amounts of TE- and TM-like radiation in the guide were not exactly equal. Extinction ratios in couplers and interferometers where only the TE-like radiation is excited should be considerably higher.

A voltage difference of about 25 V is required to produce a π phase shift in the TE-like mode, i.e., to go from a maximum to a minimum in the relative output of either curve shown in Figure 1-11. Using simple approximations for both the electric field shape in the p-n junction and the field shape of the TE-like optical mode, a rough estimate of $\approx 1.5 \times 10^{-10}$ cm V for the electrooptic coefficient n_{41} was obtained from the measured voltage difference. This value is in reasonable agreement with the n_{41} value of 1.3×10^{-10} cm V reported for InP at 1.35 μ m by Tada and Suzuki.²⁸

J.P. Donnelly	F.J. O'Donnell
N.L. DeMeo	S.H. Groves

REFERENCES

1. A.R. Clawson, D.P. Mullin, D.I. Elder, and H.H. Wieder, *J. Cryst. Growth* **64**, 90 (1984).
2. Solid State Research Report, Lincoln Laboratory, M.I.T. (1984:3); S.H. Groves, V. Diadiuk, M.C. Plonko, and D.L. Hovey (to be published in *Appl. Phys. Lett.*, January 1985).
3. C.H. Cox, III (unpublished).
4. D. Yap and L.M. Johnson, *Appl. Opt.* **23**, 2991 (1984).
5. L.M. Johnson and D. Yap, *Appl. Opt.* **23**, 2988 (1984).
6. Solid State Research Report, Lincoln Laboratory, M.I.T. (1983:1), p. 7. DTIC AD-A128894 3.
7. *Ibid.* (1984:2), p. 7, DTIC AD-A147640.
8. K. Utaka, S. Akiba, K. Sakai, and Y. Matsushima, *IEEE J. Quantum Electron.* **QE-20**, 236 (1984), and references therein.
9. Y. Itaya, T. Matsuoka, K. Kuroiwa, and T. Ikegami, *IEEE J. Quantum Electron.* **QE-20**, 230 (1984), and references therein.
10. H. Okuda, Y. Hirayama, J. Kinoshita, H. Furuyama, and Y. Uematsu, *Electron. Lett.* **19**, 941 (1983).
11. L.D. Westbrook, A.W. Nelson, P.J. Fiddymont, and J.S. Evans, *Electron. Lett.* **20**, 225 (1984).
12. M. Kitamura, M. Yamaguchi, S. Murata, I. Mito, and K. Kobayashi, *Electron. Lett.* **20**, 595 (1984), and references therein.
13. B. Broberg, F. Koyama, Y. Tohmori, and Y. Suematsu, *Electron. Lett.* **20**, 692 (1984).
14. Z.L. Liao and J.N. Walpole, *Appl. Phys. Lett.* **40**, 568 (1982). DTIC AD-A121779.
15. Z.L. Liao, J.N. Walpole, and D.Z. Tsang, *IEEE J. Quantum Electron.* **QE-20**, 855 (1984).
16. D.C. Flanders, *J. Vac. Sci. Technol.* **16**, 1615 (1979), DTIC AD-A090070 4.
17. N.L. DeMeo, J.P. Donnelly, F.J. O'Donnell, M.W. Geis, and K.J. O'Connor, presented at the Conference on Ion-Beam Modification of Materials '84, Ithaca, New York, 1984; to be published in *Nucl. Instrum. Meth.*
18. A.W. Nelson, L.D. Westbrook, and J.S. Evans, *Electron. Lett.* **19**, 34 (1983).

19. J. Kinoshita, H. Okuda, and Y. Uematsu, *Electron. Lett.* **19**, 215 (1983).
20. The present calculation is somewhat different from that in Reference 15 because of the device geometry and the relative importance of the electron drift current.
21. A. Carengo, L. Menegaux, and N.T. Lenh, *Appl. Phys. Lett.* **40**, 653 (1982).
22. F.J. Leonberger, J.P. Donnelly, and C.O. Bozler, *Appl. Phys. Lett.* **29**, 652 (1976), DDC AD-A037627/7.
23. J.P. Donnelly, N.L. DeMeo, G.A. Ferrante, K.B. Nichols, and F.J. O'Donnell, *Appl. Phys. Lett.* **45**, 360 (1984).
24. J.P. Donnelly, N.L. DeMeo, G.A. Ferrante, and K.B. Nichols, "A High Frequency GaAs Optical Guided Wave Electrooptic Interferometric Modulator" (to be published in *IEEE J. Quantum Electron.*).
25. J.P. Donnelly and C.A. Armiento, *Appl. Phys. Lett.* **34**, 96 (1979), DTIC AD-A069910/8.
26. S. Namba, *J. Opt. Soc. Am.* **51**, 76 (1961).
27. A. Yariv, *Quantum Electronics* (Wiley, New York, 1967), pp. 300-306.
28. K. Tada and N. Suzuki, *Jpn. J. Appl. Phys.* **19**, 2295 (1980).

2. QUANTUM ELECTRONICS

2.1 EVALUATION OF THE Nd:Cr:GSGG LASER

Research on the Nd:Cr:GSGG laser described previously¹ has continued; this report will discuss determination of crystal losses, a comparison with the Nd:YAG laser, measurements of thermal lensing, and operation in the 1300-nm-wavelength region.

The loss in a solid state laser cavity associated with the laser rod can be estimated by evaluating the laser output as a function of both the pump input and the output mirror transmission. In a pulsed system, the output energy E_{out} is well approximated by the expression

$$E_{out} = \Delta(E_{in} - E_{th}) \quad (2-1)$$

where E_{in} is the pump energy, E_{th} is the pump input energy at threshold, and Δ is the slope efficiency. Δ is in turn approximated by

$$\Delta = \frac{\Delta_o T}{L + T} \quad (2-2)$$

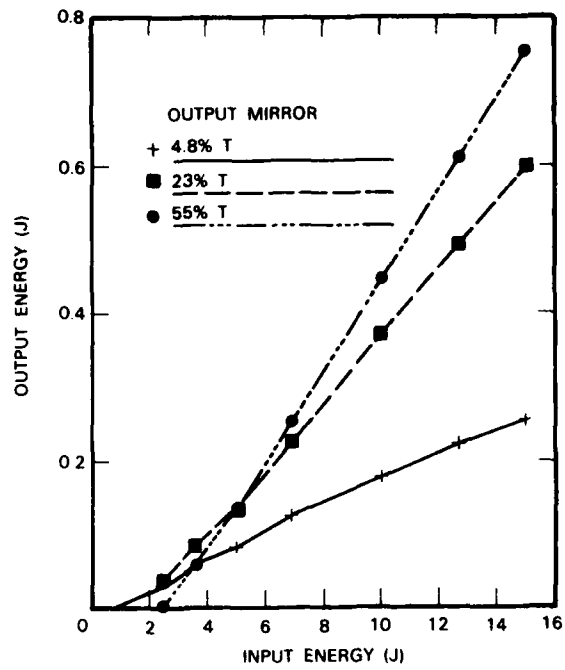
where T is the output-mirror fractional transmission, and L is the round-trip fractional loss in the laser cavity not associated with the output mirror. Δ_o is the limiting slope efficiency in the system, related to the overall conversion of pump input energy to stored energy in the upper laser level. Measurements of Δ at several values of T allow the calculation of both L and Δ_o , by taking ratios between observed slope efficiencies.

Data on the input-output performance at 1060 nm of a 0.5×7.5 -cm Nd:Cr:GSGG rod for three output-mirror transmissions is shown in Figure 2-1. The boule from which the rod was fabricated was determined by optical absorption measurements[†] to be doped with approximately 1.5×10^{20} Nd³⁺ ions/cm³ (0.65 wt%) and 7.5×10^{19} Cr³⁺ ions/cm³ (0.15 wt%). The 400-Torr-pressure xenon pump-lamp had an arc length of 6.4 cm, a bore diameter of 0.4 cm, and a Ce-doped quartz envelope; the pump cavity was a Kigre[‡] YW-525 doped-glass assembly. The LC-discharge network had capacitance and inductance values of 55 μ F and 82 μ H, respectively.

Analysis of the data in Figure 2-1 showed that L was 0.10 and Δ_o was 0.07. The three different possible values for L calculated by taking ratios of slopes all agreed within ± 10 percent. The resultant loss in the laser rod is equivalent to an absorption/scattering loss coefficient of ~ 0.007 cm⁻¹. The same series of slope measurements was performed on a conventional 1%-doped Nd:YAG laser rod, and the resultant values for L and Δ_o were 0.075

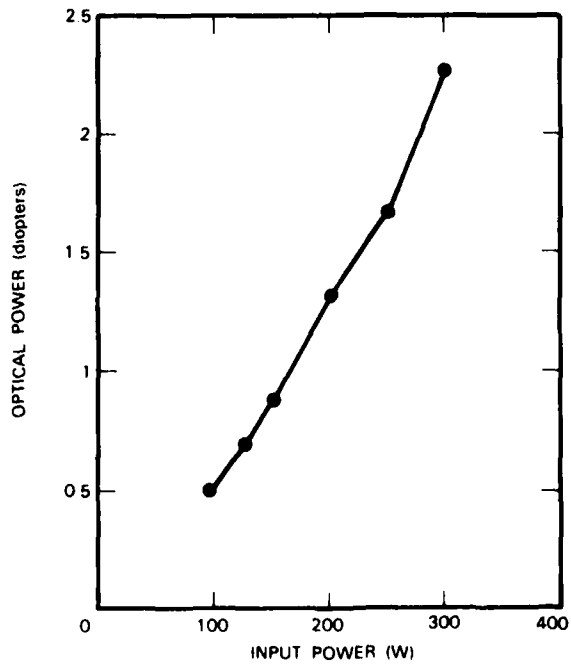
[†] The assistance of Dr. Michael Shinn at Lawrence Livermore Laboratory in these measurements is acknowledged.

[‡] Kigre Inc., Toledo, Ohio.



148307 N

Figure 2-1. Input-output energy curves at 1060 nm for the Nd:Cr:GSGG laser for three different output-mirror transmissions.



148308 N

Figure 2-2. Thermal lens created by pumped Nd:Cr:GSGG rod as a function of average power to pump lamp. Lamp pulse rate was 10 Hz.

and 0.039, respectively. Thus, the particular rod of Nd:Cr:GSGG used in the experiments increased the limiting slope efficiency by a factor of 1.8 over a Nd:YAG rod.

Thermal lensing in the Nd:Cr:GSGG rod as a function of average pump power was measured by passing a collimated beam from a 1.15- μm helium-neon laser through the pumped rod and determining the position of the beam focus. Data are shown in Figure 2-2, where the thermal focal length is expressed in diopters, the inverse of the focal length in meters. The thermal focal length of a Nd:YAG rod under the same conditions was considerably greater and difficult to determine; it was roughly ten times larger. Thus, the increased efficiency from Nd:Cr:GSGG is accompanied by a much greater thermal-lensing effect, even at the same output level.

Operation of the Nd:Cr:GSGG laser on the ${}^4F_{3/2} \rightarrow {}^4I_{13/2}$ transition in the 1300-nm-wavelength region was obtained by appropriately changing both the AR coatings on the rod and the laser-cavity mirrors. Input-output data appear in Figure 2-3 for two different output-mirror transmissions. The values for L and Δ_0 (calculated similarly as above for 1060-nm operation) were 0.08 and 0.048, respectively.

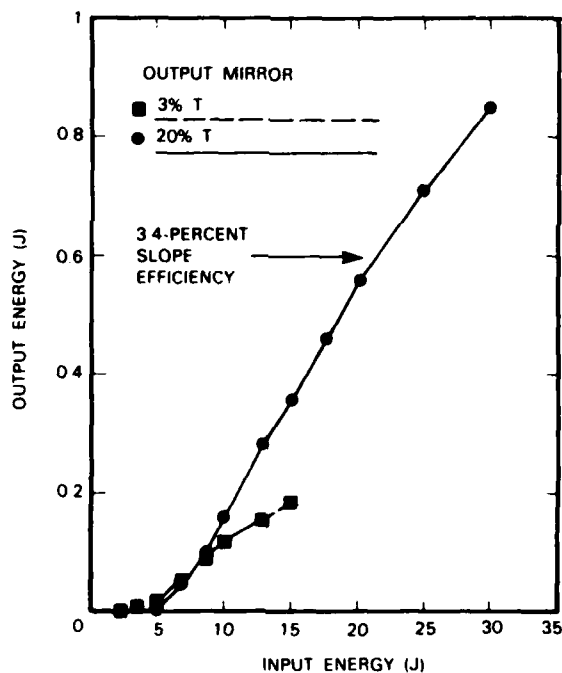


Figure 2-3. Input-output energy curves for 1300-nm operation of Nd:Cr:GSGG laser, at two different output-mirror transmissions.

In summary, the Nd:Cr:GSGG laser has a greater slope efficiency than the Nd:YAG system, but also a considerably greater thermal-lensing effect. Thus, more efficient Nd³⁺ lasers can be constructed using the Cr³⁺-sensitized GSGG host, but the laser cavity design will have to compensate for a relatively high value of thermal lensing if a rod geometry is employed. Efficient 1300-nm operation of Nd:Cr:GSGG has been demonstrated, with possible application as a pump source for Co²⁺ or Ni²⁺ doped lasers.

P.F. Moulton

2.2 ENHANCED QUANTUM EFFICIENCY INTERNAL PHOTOEMISSION DETECTORS BY GRATING COUPLING TO SURFACE PLASMA WAVES

The use of gratings to couple optical energy into surface plasma-wave modes that are confined to a metal-dielectric boundary has been extensively explored.² With optimal choices of the grating period and profile, nearly 100-percent coupling efficiency has been achieved.³ This coupling has been used to enhance the quantum efficiency of internal photoemission detectors in which hot carriers are generated in a metal film by optical absorption, and are collected by internal photoemission over a Schottky barrier into a semiconductor. There has been significant interest⁴⁻⁶ in internal photoemission detectors as a result of their uniformity, long wavelength response, and compatibility with integrated-circuit fabrication techniques.

For these initial experiments the Au-(p-InP) system was used. Gratings with a period of 2 μm and a line/space ratio of $\sim 1/3$ were fabricated photolithographically on heavily doped ($\sim 1 \times 10^{18} \text{ cm}^{-3}$) p-InP. Electron-beam evaporated Au films were deposited to form the Schottky barriers. Both the film thickness and the groove depth were varied to find the optimum coupling conditions. Detectors were defined by removing most of the Au film, leaving square areas 125 μm on a side. Thicker Au contact pads were evaporated along one edge of the detector; the ohmic back contact was thermally evaporated AuMg alloyed at 420°C for 10 s.

Both CW 1.15- μm He-Ne and mode-locked 1.06- μm YAG lasers were used to characterize the detector performance. Figure 2-4 shows the reflectivity (top trace) and the detector response (bottom trace) as a function of the angle of incidence for 1.15- μm irradiation of a detector with 50-nm-deep grooves and a 30-nm-thick Au film. These curves are for TM polarization, with the grating grooves oriented perpendicular to the electric field vector. The dips in the reflectivity at incident angles of 26°, 8°, and 45° correspond to the $m = 1, 2,$ and 3 surface plasma wave coupling resonances, respectively. The decreases in the reflectivity near normal and grazing incidence are due to experimental limitations. The small peaks in the reflectivity curve near 18° and 35° are not actual changes in the reflectivity (zero-order diffraction) but are due to higher-order diffracted beams which are scattered into the collection optics at these angles.

The corresponding responsivity results for this detector, as well as those for an identically fabricated detector without the grating morphology, are shown in the bottom trace of

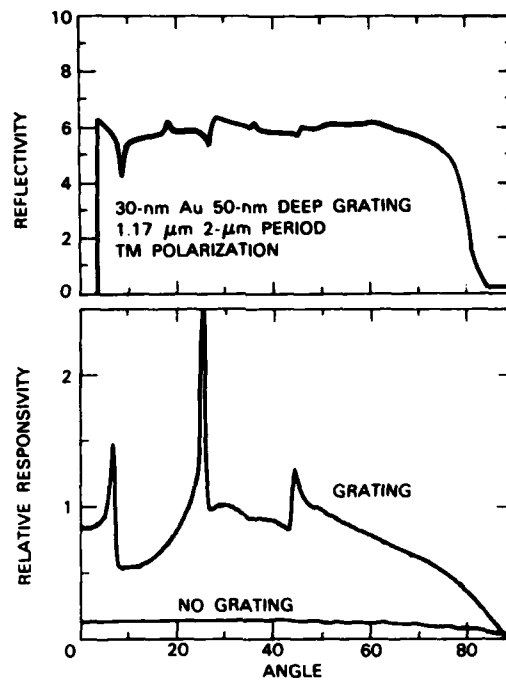


Figure 2-4. Reflectivity (top) and detector response (bottom) as incident angle is varied for TM-polarized, 1.15- μm radiation incident on an Au-(p-InP) Schottky-barrier internal photoemission detector with an etched surface grating (see text for details). Dips in reflectivity and corresponding peaks in response occur at angles for coupling into surface plasma waves at air-metal interface.

Figure 2-4. The three peaks in the response correspond to the dips in the reflectivity. At the resonant coupling angles, more of the incident energy is coupled into the surface plasma wave mode at the air-Au interface, is absorbed in the metal, and ultimately contributes to the detector response. The maximum responsivity, at the peak of the $m = 1$ resonance, is a factor-of-30 greater than the responsivity for the untextured detector. The quantum efficiency at this angle was ~ 0.4 percent at zero bias. This increased to 1.2 percent at a reverse bias of 2 V, probably because of both field-induced tunneling and field-induced depression of the Schottky barrier in this heavily doped substrate. Peak quantum efficiencies of over 2 percent at reverse biases of 3 V were observed with somewhat more deeply etched gratings.

By varying both the groove depth and the film thickness, very different angular response patterns were generated. For 100-nm-deep grooves, the response did not show the sharp peaks illustrated here but rather consisted of flat plateaus with significant changes in the response at the positions corresponding to the peaks in the 50-nm-deep groove detectors. The peak response occurred at normal incidence and extended for a total angular acceptance of $\sim 20^\circ$.

The resonant coupling angles can be simply evaluated from the relation:

$$\theta = \sin^{-1} \left\{ \operatorname{Re} \sqrt{\frac{\epsilon}{\epsilon + 1}} - m \frac{\lambda}{d} \right\} \quad (2-3)$$

where ϵ is the metal dielectric constant, and d is the grating period. The finite thickness of the metal film causes some broadening and shifting of the resonance positions. A more detailed analysis of this response has been carried out and will be reported elsewhere.⁷

The response speed of these detectors is limited by the RC time constant associated with the capacitance of the Schottky barrier and by the hot-carrier transit time across the depletion region. For this heavily doped substrate material, the capacitance limit is much more severe since the depletion region is only ~ 30 nm wide at zero bias. The detector response speed was measured using 100-ps-duration 1.06- μm pulses from a CW mode-locked YAG laser. At zero bias, the detector fall time of 3.7 ns was consistent with the measured capacitance. This response time decreased to less than 2 ns at a reverse bias of 3 V as a result of the increased depletion width. By properly choosing the substrate carrier concentrations and detector dimensions, it should be possible to construct detectors with response speeds of ~ 10 ps without any loss in responsivity.

Further optimization of the detector response should result in higher quantum efficiency and higher speed. Significantly better responsivity can be achieved by using a higher spatial frequency grating so that only one diffracted order is allowed. In this case, all the energy coupled out of the incoming light beam is converted to surface waves and ultimately to hot carriers; for the present relatively coarse grating ($\lambda/d = 0.59$), some of the energy is merely shifted between the reflected and transmitted beams and the various diffracted orders, and reradiated. Model calculations indicate that only approximately 1/3 of the energy coupled out of the reflected beam is actually absorbed in the metal. Fabrication of a much higher spatial frequency grating ($d \sim \lambda/n$, where n is the semiconductor refractive index) and illumination through the semiconductor material will allow coupling to the surface plasma wave at the metal-semiconductor interface. Because the energy in this mode is closely confined to the interface, the quantum efficiency would be increased, as carriers would not have to diffuse across the metal film before collection.

We have demonstrated improved quantum efficiencies for internal photoemission detectors in the Au-InP system through grating coupling of incident radiation into surface plasma wave modes. These same techniques are also applicable to other Schottky-barrier systems such as metal-GaAs and metal or metal silicide-Si. For the GaAs case, this will result in a fast detector for the near-infrared wavelengths used in low-loss fiberoptic systems that can be fabricated on bulk GaAs and is compatible with additional GaAs integrated-circuit construction. For many of the metal silicide-Si systems, techniques such as back illumination and resonant cavity overlayers have already been developed⁴⁻⁶ to provide high absorption

efficiencies in the thin metallic layers; nevertheless, the capability to tailor the spectral response by adjusting the grating parameters will provide enhanced capabilities, particularly for the detection of spectrally narrow sources.

S.R.J. Brueck T. Jones
V. Diadiuk W. Lenth

2.3 THEORY OF THE EFFECT OF TRAPS ON THE SPECTRAL CHARACTERISTICS OF DIODE LASERS

According to the Schawlow-Townes theory,⁸ the power spectrum of a laser is Lorentzian and the linewidth $\Delta\omega$ extrapolates to zero in the limit of high-power output P. For GaAs/GaAlAs heterostructure diode lasers, the observed spectra are approximately Lorentzian. However, the measured full width at half maximum is given by $\Delta\omega = (\Delta\omega)_{ST} + (\Delta\omega)_e$, where the Schawlow-Townes linewidth $(\Delta\omega)_{ST}$ varies as $1/P$, and the excess linewidth $(\Delta\omega)_e$ is power independent but strongly temperature dependent.⁹ For such lasers the measured FM noise spectrum,^{10,11} which is related to the lineshape,¹¹ has a low-frequency component varying as $\sim 1/f$. Since many theoretical accounts of $1/f$ current fluctuation noise in semiconductors involve the presence of trap levels, these diode-laser characteristics suggest that a theory of laser operation in the presence of traps might prove fruitful. We have developed such a theory, which can account for the excess linewidth and provides a unified description of the FM noise spectrum and the current noise spectrum as well as the lineshape.

The basis of the theory is the solution of the set of semiclassical linearized equations of motion of fluctuating system variables under the influence of Langevin forces.¹² The equations describing the fluctuations in phase and amplitude of the laser are modifications of those used by Vahala and Yariv¹³ and others.¹⁴ The coupling of electromagnetic fluctuations to trap population fluctuations occurs via the change in dielectric constant with trap occupation. To obtain linearized coupled equations describing the rate of change of fluctuations in the populations of conduction electrons and trapped electrons, the equations given by Lax¹² are modified to take account of the effect of stimulated emission. The linearized coupled equations are then solved by matrix methods, and the solutions are used to compute time-dependent correlation functions that are related to the measured diode-laser characteristics.

The laser FM noise spectrum is proportional to the spectral density calculated from the correlation function $\langle \dot{\phi}(\tau)\dot{\phi}(0) \rangle$:

$$S(\dot{\phi}, \omega') = \int_{-\infty}^{\infty} \langle \dot{\phi}(\tau)\dot{\phi}(0) \rangle \exp[-i\omega'\tau] d\tau \quad (2-4)$$

where ϕ is the fluctuating phase, ω' is the angular frequency, and $\langle \rangle$ denotes an ensemble average. For the frequency range of interest, the spectral density obtained by using our theory to evaluate the right side of Equation (2-4) is

$$S(\dot{\phi}, \omega') = U_{11}(1 + \alpha^2) + \frac{1}{2} \left(\frac{\Gamma\omega_0\xi_\mu}{\epsilon} \right)^2 \langle \delta n_\mu \delta n_\mu \rangle \frac{A_{\mu\mu}}{(\omega'^2 + \Lambda_{\mu\mu}^2)} \quad (2-5)$$

where summation over repeated indices is implied. The first term on the right side of Equation (2-5), which is due to fluctuations in the laser phase and amplitude¹³ and contributes a white-noise component to the FM spectrum, is equal to $(\Delta\omega)_{ST}$. The second term is due to fluctuations in the number of electrons occupying traps that communicate with the conduction band in the active region. In this term Γ is a filling factor, ω_0 is the center angular frequency of the laser, ϵ is the real part of the dielectric constant, n_μ is the number of electrons occupying the μ^{th} species of trap, δn_μ is a fluctuation in n_μ , $\xi_\mu \equiv (\partial\epsilon/\partial n_\mu)$, and $\Lambda_{\mu\mu}$ is the decay rate for the μ^{th} trap species.

For a region with a more-or-less uniform spatial distribution of traps, if communication between the traps and a conduction band takes place via tunneling through a potential barrier, the rate of decay is exponentially dependent on tunneling distance,¹⁵ yielding a distribution of decay rates $\rho(\Lambda_{\mu\mu}) \equiv dn_\mu/d\Lambda_{\mu\mu} = c/\Lambda_{\mu\mu}$. For such a distribution, the second term on the right side of Equation (2-5) will lead to a $1/f$ contribution to the FM spectrum, if ξ_μ and $\langle\delta n_\mu\delta n_\mu\rangle$ do not vary strongly with the trap species. It has been established experimentally that trapping centers with a range of Λ values are present in the GaAlAs confining layers adjacent to the active region of heterostructure diode lasers.¹⁶ The measured Λ values vary from ~ 0.1 to ~ 10 s^{-1} , the upper limit that could be determined by the experimental technique used. If the Λ values extend to $\sim 10^5$ s^{-1} , these traps could account for the observed $1/f$ component of the FM spectrum. As discussed below, we postulate additional traps with a different Λ distribution that contribute to the nearly flat portion of the FM spectrum observed beyond the $1/f$ region.

The laser power spectrum is related to the correlation function $\langle[\phi(\tau) - \phi(0)]^2\rangle$ by the expression

$$S_P(\omega) = \int_{-\infty}^{\infty} \exp\left\{-\frac{1}{2} \langle[\phi(\tau) - \phi(0)]^2\rangle\right\} \exp\{-i(\omega - \omega_0)\tau\} d\tau. \quad (2-6)$$

We have shown that the general expressions given by our theory for this correlation function and for the FM noise spectrum satisfy the basic relationship between these quantities derived by Walther and Kaufmann¹¹

$$\langle[\phi(\tau) - \phi(0)]^2\rangle = |\tau|^2 \int_{-\infty}^{\infty} \frac{\sin^2 u}{u^2} S(\dot{\phi}, \omega') \frac{d\omega'}{2\pi} \quad (2-7)$$

where $u \equiv (\omega|\tau|)/2$. Therefore, once $S(\dot{\phi}, \omega')$ is evaluated, either experimentally or theoretically, the correlation function can be calculated from Equation (2-7) and $S_P(\omega)$ can then be calculated from Equation (2-6).

When the line shape of a diode laser is calculated from experimental data^{10,11} for $S(\dot{\phi}, \omega')$ by using Equations (2-6) and (2-7), it is found that in the vicinity of the half-power point ($\omega_{1/2} = \omega_0 + \Delta\omega/2$) the main contribution to $S_P(\omega)$ arises from $S(\dot{\phi}, \omega')$ in the vicinity of $\omega' = \Delta\omega/2$. The measured values of $\Delta\omega/2$ fall in the range from $\sim 3 \times 10^6$ to $\sim 3 \times 10^7$ s^{-1} , where the $1/f$ component of $S(\dot{\phi}, \omega')$ is negligible. If the trap term in Equation (2-5)

was due entirely to traps of the type discussed previously, with Λ values extending no higher than 10^5 s^{-1} , only $U_{11}(1 + \alpha^2)$ would contribute to the power in the vicinity of $\omega_{1/2}$. In that case, the spectrum in this region would be Lorentzian with no excess linewidth. To account for the observed spectrum, which is Lorentzian but has a finite value of $(\Delta\omega)_e$, we postulate an additional set of traps (designated by d), all of which have values of Λ large enough compared with $\Delta\omega/2$ to make an appreciable contribution to $S(\dot{\phi}, \omega')$ in the vicinity of $\omega' = \Delta\omega/2$. Their total contribution in this region, as given by the trap term in Equation (2-5), is frequency independent (since $\Lambda_{dd}^2 \gg \omega'^2$) and yields the excess linewidth

$$(\Delta\omega)_e = \frac{1}{2} \left(\frac{\Gamma\omega_0\xi_d}{\epsilon} \right)^2 \langle \delta n_d \delta n_d \rangle \frac{1}{\Lambda_{dd}} \quad (2-8)$$

We suggest that the additional traps are the relatively shallow dopant impurities located in the laser active region. The large increase observed⁹ in $(\Delta\omega)_e$ as the temperature is decreased from room temperature to 1.7 K could then be attributed to the increase in the number of electrons occupying these impurity levels.

At present Equation (2-8) cannot be used to calculate $(\Delta\omega)_e$ from experimental quantities, since ξ_d , $\langle \delta n_d \delta n_d \rangle$, and Λ_{dd} are not known. However, upper limits on $(\Delta\omega)_e$ can be estimated by making the reasonable assumptions that $\xi_d < \xi$ (where $\xi \equiv \partial\epsilon/\partial n$ and n is the number of conduction electrons), $\langle \delta n_d \delta n_d \rangle < n_d$, and $\Lambda_{dd} \approx 10^8 \text{ s}^{-1}$. Using measured values of ξ and n_d over the temperature range from 300 to 1.7 K, we obtain upper limits for $(\Delta\omega)_e$ that are comfortably higher than the measured values.

The qualitative effects on the FM noise spectrum of the two types of traps that we have postulated are illustrated by Figure 2-5, which is a highly schematic log-log plot of

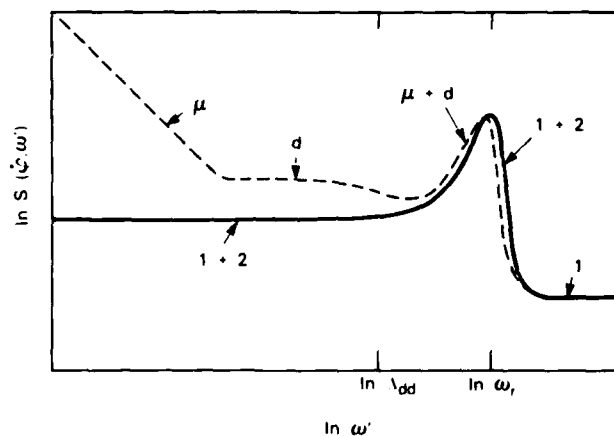


Figure 2-5. Schematic plot of FM noise spectrum of diode laser for trap model discussed in text. Solid line is sum of contributions due to fluctuations in laser phase and amplitude (designated by 1 and 2, respectively). Dashed line is total spectrum obtained by adding contributions of traps designated as μ and d.

$S(\phi, \omega')$ vs ω' . In the absence of the traps, the spectrum would have the form shown by the solid line, which is the sum of contributions due to fluctuations in the laser phase and amplitude (designated in the figure by 1 and 2, respectively). This line consists of an initial flat portion, a peak centered at the relaxation frequency ω_r that is associated with the resonant coupling between the laser emission and the conduction electrons,^{13,14} and a final flat portion due to fluctuations in phase only. The dashed line in Figure 2-5 shows the total spectrum obtained when the contributions of the two types of traps (designated by μ and d) are added. In addition to the $1/\omega$ and frequency-independent components due to the μ and d traps, respectively, this spectrum shows a small shift in the position of the resonant peak that reflects a joint contribution from both types of traps.

H.J. Zeiger

REFERENCES

1. Solid State Research Report, Lincoln Laboratory, M.I.T. (1984:1), pp. 7-9, DTIC AD-A147429.
2. A.A. Maradudin, in *Surface Polaritons*, V.M. Agranovich and D.L. Mills, Eds. (North-Holland, New York, 1982), p. 405.
3. I. Pockrand, *J. Phys. D* **9**, 2423 (1976).
4. F.D. Shepherd, in *Infrared Detectors*, W.L. Wolfe, Ed., Proc. SPIE **43**, 42 (1984).
5. W.F. Kosonocky and H. Elabd, *ibid.*, p. 167.
6. R.C. McKee, *IEEE Trans. Electron Devices* **ED-31**, 968 (1984).
7. S.R.J. Brueck, V. Diadiuk, T. Jones, and W. Lenth (to be published).
8. A.L. Schawlow and C.H. Townes, *Phys. Rev.* **112**, 1940 (1958).
9. D. Welford and A. Mooradian, *Appl. Phys. Lett.* **40**, 560 (1982); J. Harrison and A. Mooradian, *Appl. Phys. Lett.* **45**, 318 (1984).
10. A. Dandridge and A.B. Tveten, *Appl. Phys. Lett.* **39**, 530 (1981).
11. F.G. Walther and J.E. Kaufmann, Topical Meeting on Optical Fiber Communication, New Orleans, Louisiana, 26 February — 2 March 1983, Technical Digest, p. 70.
12. M. Lax, *Rev. Mod. Phys.* **32**, 25 (1960).
13. K. Vahala and A. Yariv, *IEEE J. Quantum Electron.* **QE-19**, 1102 (1983).
14. B. Daino, P. Spano, M. Tamburrini, and S. Piazzola, *IEEE J. Quantum Electron.* **QE-19**, 266 (1983).
15. A.L. McWhorter, *Phys. Rev.* **98**, 1191 (1955).
16. T. Matsumoto and P.K. Bhattacharya, *Appl. Phys. Lett.* **42**, 52 (1983).

3. MATERIALS RESEARCH

3.1 IMPURITIES IN POLYCRYSTALLINE InP INGOTS

To prepare starting material for the growth of InP single crystals by the liquid-encapsulated Czochralski (LEC) method, polycrystalline InP is synthesized from the elements in the form of n-type ingots produced by directional solidification of In-rich solutions under controlled P pressure in fused-silica ampoules. Ingots with large enough grain size are characterized by making Hall coefficient (R_H) and resistivity (ρ) measurements on rectangular single-crystal bars with dimensions of at least $1 \times 2 \times 10$ mm. The electron concentration at 300 K (n_{300}) is calculated from $n = e^{-1} R_H^{-1}$, and the Hall mobility at 77 K (μ_{77}) from $\mu = R_H \rho^{-1}$. As reported earlier,[†] photoluminescence data at high magnetic fields show that S is the dominant shallow donor impurity in high-purity ingots, for which $n_{300} \leq 2 \times 10^{15} \text{ cm}^{-3}$ and $\mu_{77} \geq 5 \times 10^4 \text{ cm}^2 \text{V}^{-1} \text{s}^{-1}$.

Fifteen polycrystalline InP ingots, each weighing about 1 kg, were synthesized during 1984. Table 3-1 lists in chronological order each of the 12 ingots for which electrical measurements could be made, together with the lots of In and P used, the synthesis parameters, and the values of n_{300} and μ_{77} for a sample cut from near the first-to-freeze end of the ingot. The distributions of the μ_{77} values measured for such samples from 1980 through 1984 are shown in histogram form in Figure 3-1. From this figure, it is evident that there was a significant reduction in the yield of high-purity ingots during 1983 and especially 1984. Thus, the fraction of ingots with $\mu_{77} > 5 \times 10^4 \text{ cm}^2 \text{V}^{-1} \text{s}^{-1}$ was 23/44 for 1980 through 1982, 7/20 in 1983, and only 2/12 in 1984. Note that the P was vacuum baked in the synthesis ampoule before InP synthesis for all the 1984 ingots and most of the 1983 ingots, but not for any of the 1980-82 ingots.

We attribute the reduction in the yield of high-purity ingots basically to a decrease in the purity of the as-received P used as starting material. This explanation is supported by the observation of significant differences in purity between ingots prepared from the same lot of In but different lots of P, increases in purity achieved by P prebaking, and a striking correlation between purity and ampoule design for ingots synthesized during 1983 and 1984. Two different designs, which we designate as "design 1" and "design 2," were used for these ingots. As shown in Figure 3-1, high-purity ingots were obtained only when P prebaking was employed in ampoules with design 2. After this correlation was found, we realized that because of the configurations of the ampoule pumping ports the effectiveness of prebaking in removing volatile impurities from the P should be greater for design 2 than for design 1. This difference can explain the correlation if the impurities originate in the P.

[†] Solid State Research Report, Lincoln Laboratory, M.I.T. (1984:1), p. 25, DTIC AD-A147429.

TABLE 3-1 Synthesis Parameters and Electrical Properties of Polycrystalline InP Ingots Prepared in 1984											
Ingot	Indium			Phosphorus				Ampoule Design	InP		
	Source, Lot	Vacuum Bake (°C, h)	Maximum Boat Temperature (°C)	Source, Lot	Vacuum Bake (°C, h)	Synthesis Temperature (°C)	n ₃₀₀ (10 ¹⁵ cm ⁻³)		μ ₇₇ (10 ⁴ cm ² V ⁻¹ s ⁻¹)		
84-1	ICA, A1236	900, 6	1060	MCP, 83/01	250, 6	460	1	33	1.2		
84-2	ICA, A1236	900, 6	1060	MCP, 83/01	250, 6	460	1	19	1.8		
84-3	ICA, A1236	900, 6	1060	RASA, 20230	300, 3 200, 4 100, 100	460	2	0.4	9.1		
84-4	ICA, A1236	900, 6	1060	MCP, 83/01	300, 5 200, 72	460	2	1.5	6.4		
84-5	ICA, A1236	900, 6	1060	MCP, 8305	300, 5	460	1	19	1.4		
84-6	ICA, A1236	900, 6	1060	MCP, 8305	300, 5	460	1	19	1.5		
84-7	ICA, A118	900, 6	1060	MCP, 7403	200, 6	460	2	6.4	3.0		
84-8	ICA, JK595	900, 6	1060	MCP, 7403	235, 2 180, 24	460	1	3.8	2.5		
84-9	ICA, JK595	900, 6	1060	MCP, 8307	140, 6	460	1	11	2.0		
84-10	MCP, HR312	900, 6	1060	MCP, 8307	230, 16	460	2	16	1.6		
84-11	MCP, HR312	900, 6	1065	MCP, 7401	170, 7	467	2	16	1.4		
84-12	MCP, HR314	900, 6	1068	MCP, 7605	170, 6	467	2	4.3	3.1		

Material Sources:

MCP — MCP Ltd.

ICA — Indium Corporation of America

RASA — RASA Industries

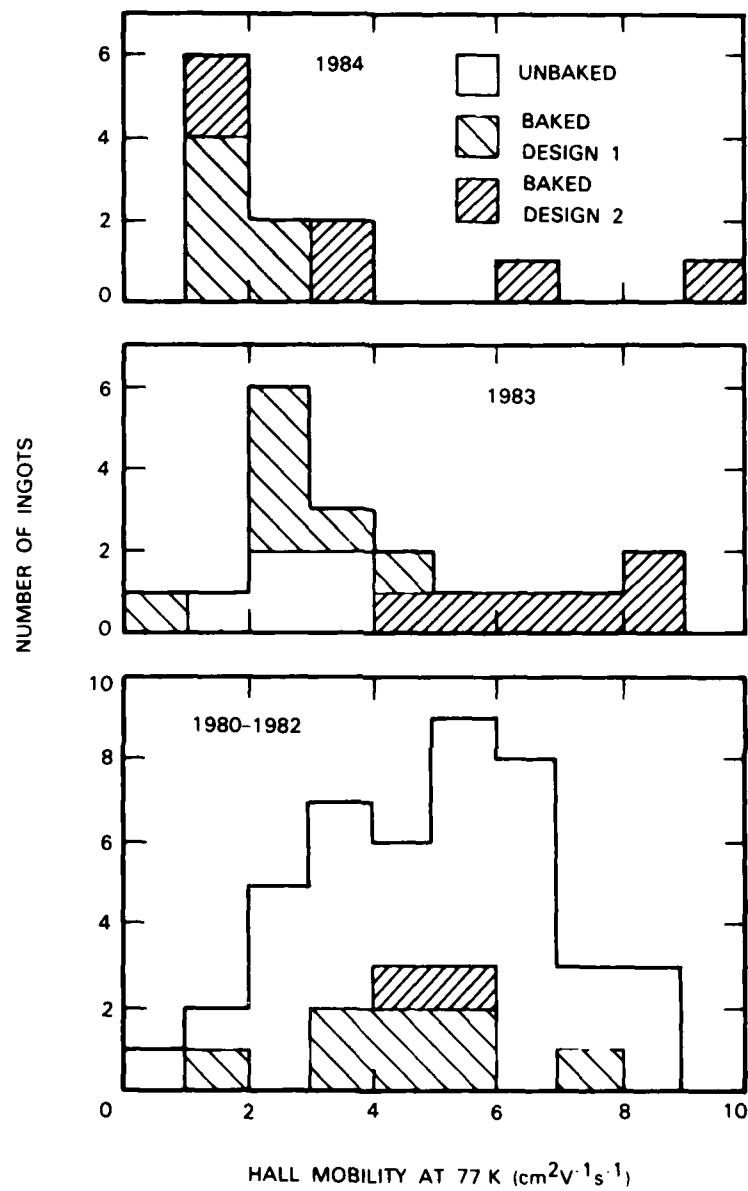


Figure 3-1. Distribution of electron Hall mobilities at 77 K for polycrystalline InP ingots.

As shown in Table 3-1, P prebaking was highly effective for the first two 1984 ingots made in ampoules with design 2, ingots 84-3 and 84-4. These ingots had μ_{77} values of 9.1 and $6.4 \times 10^4 \text{ cm}^2\text{V}^{-1}\text{s}^{-1}$, respectively, and n_{300} values of 4×10^{14} and $1.5 \times 10^{15} \text{ cm}^{-3}$. The μ_{77} value for ingot 84-3 is the highest we have ever obtained for a polycrystalline ingot, and is particularly noteworthy because ingot 83-2, which was synthesized from the same lot of P but without prebaking, had μ_{77} of only $1.1 \times 10^4 \text{ cm}^2\text{V}^{-1}\text{s}^{-1}$ and n_{300} of $2.6 \times 10^{16} \text{ cm}^{-3}$. For the four remaining ingots made in ampoules with design 2, however, the highest μ_{77} value was only $3.1 \times 10^4 \text{ cm}^2\text{V}^{-1}\text{s}^{-1}$. Apparently the P used, which came from four different lots, differed from the earlier material in such a way that the effectiveness of prebaking was substantially decreased.

The photoluminescence technique used earlier to identify donor impurities in high-purity InP samples is not applicable to samples with n_{300} greater than about $5 \times 10^{15} \text{ cm}^{-3}$. In order to identify the donor impurity of impurities present in ingots with higher values of n_{300} , six samples with $n_{300} > 1 \times 10^{16} \text{ cm}^{-3}$ (together with three control samples with $n_{300} < 1 \times 10^{15} \text{ cm}^{-3}$) were submitted to Charles Evans & Associates for determination of Si, Ge, Sn, S, Se, and Te by SIMS analysis using Cs beam excitation. The results obtained for impurities other than Si are not significant, since the concentrations found for these impurities were essentially at the respective background limits of the SIMS instrument. These limits were less than 10^{15} cm^{-3} for Ge, Se, and Te, 1 to $5 \times 10^{15} \text{ cm}^{-3}$ for S, and 1 to $3 \times 10^{16} \text{ cm}^{-3}$ for Sn. The results of the Si determinations are given in Table 3-2, where the samples are listed in order of increasing n_{300} . The data for the three purest samples establish the instrumental background limit as 1 to $2 \times 10^{15} \text{ cm}^{-3}$. The Si concentrations for the other samples are at least five times higher than this background limit. These concentrations, which are expected to be accurate to a factor of 2 or 3, are approximately equal to n_{300} for ingots 83-15 and 83-22, about $3 \times n_{300}$ for ingots 84-4 and 84-20, and about $4 \times n_{300}$ for the other two ingots. It is clear that Si, not S, is the major donor impurity in these relatively impure ingots. In addition, the data suggest that in some cases a significant fraction of the Si is not electrically active.

If the low purity of many ingots prepared during 1983 and 1984 is due to the presence of impurities that originated in the as-received P, it would follow from the SIMS results for such low-purity ingots that the dominant impurity species in the P is Si. According to this model, since the synthesis process involves the vapor transport of P from its original location in the ampoule to the boat containing molten In, incorporation of Si in the ingots would require that Si be transported through the vapor phase along with the P. However, elemental Si is far less volatile than P. The model therefore implies either that a volatile Si-bearing species is initially present in the P or that such a species is formed during the synthesis process. The existence of a Si-bearing species even more volatile than P would also account for the fact that P prebaking is sometimes very effective in improving the electrical properties of the ingots. At this time we cannot identify the hypothetical volatile Si species, although we speculate that it might be silane or some other silicon hydride. In

TABLE 3-2					
Concentrations of Si Found by SIMS Analysis					
Ingot	In (Source, Lot)	P (Source, Lot)	[Si] (10^{16} cm^{-3})	n_{300} (10^{16} cm^{-3})	[Si]/ n_{300}
83-5	ICA, A117	MCP, 8201	(0.1) [†]	0.011	—
83-4	ICA, A118	MCP, 8201	(0.2) [†]	0.058	—
83-16	MCP, HR/136	MCP, 8201	(0.2) [†]	0.14	—
83-15	MCP, HR/136	MCP, 8201	1	0.95	1
84-10	MCP, HR/312	MCP, 8307	4	1.6	2.5
83-2	ICA, A118	RASA, 20320	10	2.6	2
84-1	ICA, A1236	MCP, 83/01	10	3.3	3
83-22	MCP, HR196	RASA, 30424	4	4.2	1
82-WW	MCP, HR/134	RASA, 20320	70	16	4

Material Sources: MCP — MCP Ltd.
ICA — Indium Corporation of America
RASA — RASA Industries
† Instrumental background

addition, we cannot eliminate the possibility that the Si found in the low-purity ingots actually comes from a source other than the P. In that case, there would have to be some mechanism by which impurities in the P influence the degree to which Si in electrically active form is incorporated into the InP during synthesis.

G.W. Iseler

3.2 MICROWAVE MESFETS FABRICATED IN ZONE-MELTING-RECRYSTALLIZED Si-ON-QUARTZ FILMS

Microwave MESFETs with promising performance have been fabricated in zone-melting-recrystallized Si films on bulk fused-silica substrates. The Si-on-quartz (SOQ) structure should be useful for monolithic microwave integrated-circuit applications because of its low parasitic capacitance and the low dielectric loss of quartz. The Si films, which were $0.5 \mu\text{m}$ thick, were recrystallized in a graphite-strip-heater system by essentially the same technique

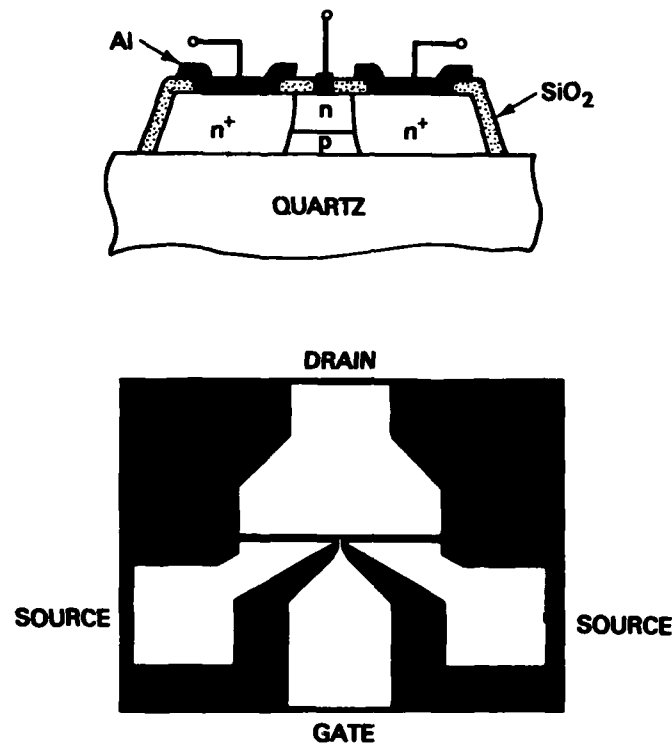


Figure 3-2. Schematic diagram and photomicrograph of Si-on-quartz microwave MESFET.

that we use for recrystallization of Si films on SiO₂-coated Si substrates.[†] Figure 3-2 shows a schematic cross section and photomicrograph of an SOQ MESFET. Because of the tensile stress incorporated during recrystallization, the SOQ films tend to crack during device processing. By using plasma etching to pattern the recrystallized films into isolated device regions, stress was greatly relieved and cracking was prevented. The channel region was doped by implantation of 80-keV P-ions to a dose of $2 \times 10^{12} \text{ cm}^{-2}$. A deep implant of 120-keV B-ions was used to provide proper channel isolation and tailor the channel thickness to $\sim 0.15 \mu\text{m}$. The source and drain were formed by P-ion implantation using photoresist as a mask. After passivation of the Si surface with a thin layer of thermal SiO₂, the Schottky gate, source, and drain contacts were fabricated by a lift-off technique with Al metallization. The devices have a gate length of $\sim 1.4 \mu\text{m}$, gate width of $200 \mu\text{m}$, and source-drain spacing of $\sim 3 \mu\text{m}$.

Figure 3-3 shows the I-V characteristics of a typical SOQ MESFET. Because of the proximity of the gate to the n⁺ source region, the Schottky diodes show a soft breakdown characteristic. This soft characteristic, along with a relatively low barrier height of 0.5 to

[†] J.C.C. Fan, B-Y. Tsaur, and M.W. Geis, *J. Cryst. Growth* **63**, 453 (1983).

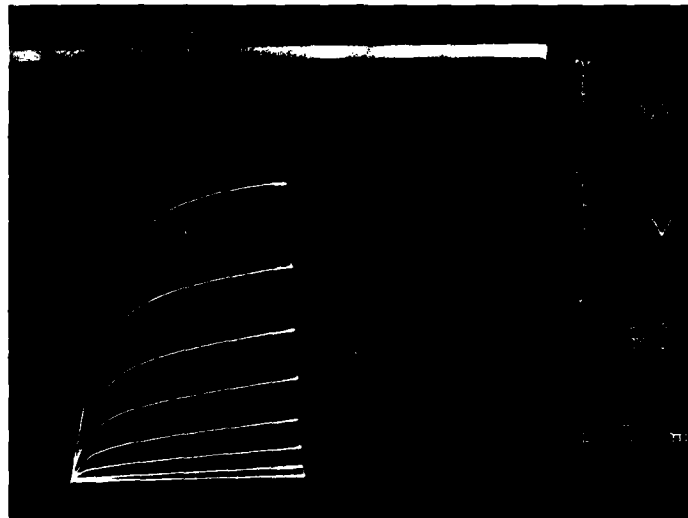


Figure 3-3. Drain I-V characteristics of SOQ MESFET.

0.6 V for the Al gate, results in incomplete turnoff of the channel region and low transconductance near the pinch-off point. However, the devices show good characteristics when operated under forward gate bias conditions and exhibit transconductance of ~ 45 mS/mm at +0.3 V gate voltage. The small pinch-off voltage of -0.5 to -0.7 V for these devices is due to the low channel doping concentration. Use of a better Schottky metallization, such as Pt or Pt silicide, and optimization of the channel doping should lead to a significant improvement in transconductance and output current capability.

Several devices have been tested for microwave performance. The maximum available power gain calculated from the measured S parameters for a typical device is shown in Figure 3-4. The data follow a 6-dB/octave decrement, consistent with the hybrid pi model. For this device the maximum frequency of oscillation f_{\max} was 9 GHz, and the maximum available gain at 2 GHz was ~ 14 dB. The best f_{\max} we have measured is ~ 14 GHz. The device of Figure 3-4 has been operated as an amplifier. The minimum noise figure was 2.5 dB at 1.2 GHz, with an associated gain of 10.4 dB. This performance is superior to that of state-of-the-art devices fabricated in silicon-on-sapphire (SOS), which employ $1\text{-}\mu\text{m}$ -gate geometry and Pt metallization.[†] We believe that reducing the gate length and optimizing other device parameters should lead to significant improvement in the microwave performance of SOQ MESFETs.

B-Y. Tsaur	C.L. Chen
H.K. Choi	R.W. Mountain
C.K. Chen	J.C.C. Fan

[†] R.J. Naster, Y.C. Hwang, and S. Zaidel, ISSCC Technical Digest, p. 72, 1981.

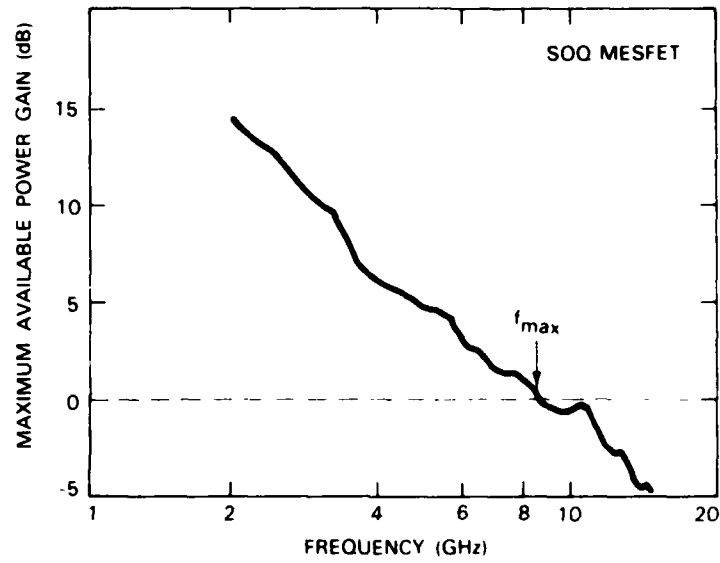


Figure 3-4. Maximum available gain as a function of frequency for SOQ MESFET.

144023-N-02

4. MICROELECTRONICS

4.1 GALLIUM ARSENIDE CHARGE-COUPLED DEVICES

We previously described a new fabrication process for an overlapping gate structure which is suitable for GaAs Schottky-barrier CCDs.¹ This process was developed to reproducibly control the gap between gate electrodes to submicrometer precision with optical lithography. Our initial results were obtained using plasma-deposited silicon nitride for the dielectric separating adjacent gates and Ti-Au for the two levels of gate metallization.¹ However, an undesirable undercutting of the silicon nitride occurs when the first-level Ti-Au gates are chemically etched with an isotropic etch, resulting in an inter-electrode gap which is larger than intended. We describe here a modified process using tungsten, which can be reactive ion etched (RIE) in CF_4 without undercutting, for the first-level metal and silicon dioxide for the dielectric. We have fabricated 16-stage CCDs with this modified process and obtained charge transfer inefficiencies (CTIs) of less than 2×10^{-4} at a 1-MHz clock rate, a result which is equal to that obtained from devices made with the previous process.

The CCDs used in this work were fabricated on n-type epitaxial GaAs grown using $\text{AsCl}_3\text{-Ga-H}_2$ vapor phase epitaxy on both Cr-doped and undoped semi-insulating substrates. The epitaxial layers were between 1.7 and 2.5 μm thick with net donor concentrations of 3 to $6 \times 10^{15} \text{ cm}^{-3}$, resulting in pinch-off voltages between 10 and 19 V. The sequence of device fabrication steps is outlined in Figure 4-1, and begins with the evaporation of 500 \AA of tungsten. Because tungsten retains good Schottky-barrier characteristics on GaAs even after anneals at temperatures as high as 800°C, there was no restriction on depositing the dielectric at low temperatures. For these devices, we used 3000 \AA of silicon dioxide pyrolytically deposited at 450°C. The first-level gates are patterned in nickel using a conventional lift-off procedure, leaving the structure shown in Figure 4-1(a). The silicon dioxide and tungsten are then etched in CF_4 using RIE with a bias of 250 V, leaving the structure depicted in Figure 4-1(b). Because the tungsten has been etched by the RIE it is not subject to undercutting, in contrast to our first process¹ in which a Ti-Au layer had to be removed by chemical etching. In the next step, the nickel RIE mask is stripped and the GaAs is given a brief chemical etch to remove the thin RIE damage before a second layer of SiO_2 with a thickness of 5000 \AA is deposited [Figure 4-1(c)]. This layer is anisotropically etched in CF_4 using RIE until the GaAs surface is again exposed, as depicted in Figure 4-1(d), leaving both the top and sides of the first-level gates covered with dielectric. The second-level gates are then produced by a Ti-Au evaporation and lift-off procedure, resulting in the structure shown in Figure 4-1(e). A scanning electron micrograph of this structure for a completed device is shown in Figure 4-2. The interelectrode gap is determined by the thickness of the second dielectric, and is approximately 5000 \AA in this case. The small undercut of the GaAs below the silicon dioxide is produced by the etch used to remove the RIE damage. Note that, if the second level metallization is sufficiently thin, the metal on the silicon dioxide will be disconnected from the metal on the GaAs. This is of importance for

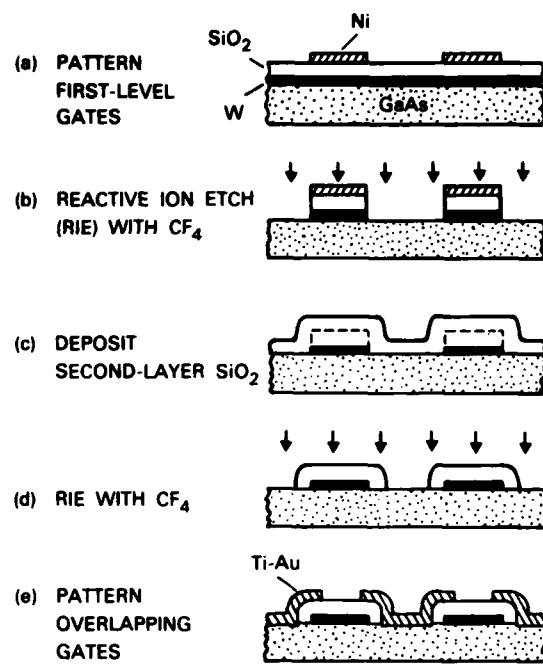


Figure 4-1. Fabrication sequence of GaAs overlapping gate CCD.

1384-N-02

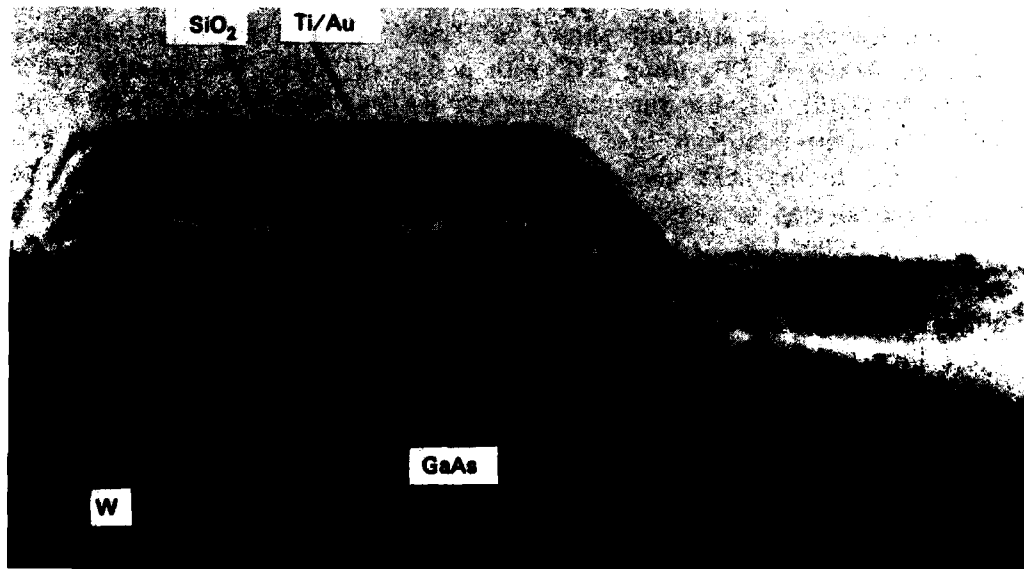


Figure 4-2. Scanning electron micrograph of overlapping CCD gates.

148474-R

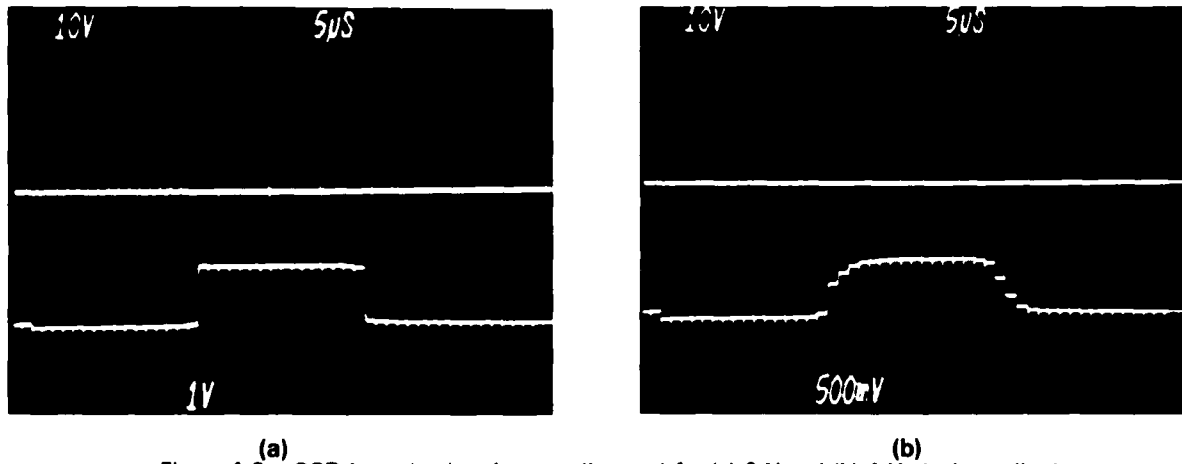


Figure 4-3. CCD input (top) and output (bottom) for (a) 6-V and (b) 4-V clock amplitude.

high-speed applications, since it would reduce the gate-to-gate capacitance to that of conventional planar CCD structures while retaining the submicrometer gap control of the overlapping gate process.

This modified process has been used to fabricate the same 16-stage, four-phase CCD structure used in the earlier work.¹ Both the first- and second-level gates consisted of 9- μm -long gates with 6- μm spaces for a 30- μm stage length. An example of device performance for a device with a 15-V pinch-off is shown in Figure 4-3, where the upper trace of each photo is a group of 16 pulses applied to the CCD input and the lower trace is the delayed CCD output. The CCD clock rate is 1 MHz, and the amplitude of clock phases 1 through 4 was 6.0 V. In Figure 4-3(a) the spacing between pulse bursts was 64 μs , and the charge loss is too small to be measured. The estimated upper limit on the transfer inefficiency is about 2×10^{-4} per transfer for the 64 transfers. This result is at least an order-of-magnitude lower than most reported CTIs for planar GaAs CCDs (see References 2 through 4) where oversized gap dimensions were cited as the principal contribution to the charge loss and is equivalent to the best CTI reported.⁵ When the clock swing is reduced below 5 V, there is an abrupt increase in CTI, as shown in Figure 4-3(b) for a clock swing of 4 V. Since this output shape has the characteristics predicted by Hansell⁶ for devices with potential troughs, we believe that the loss in Figure 4-3(b) is caused by this mechanism.

K.B. Nichols
B.E. Burke

4.2 PICOSECOND GaAs PIN PHOTODIODES

In a previous report⁷ we discussed the fabrication and characterization of a planar p-i-n photodiode that exhibits an impulse response of 19 ps FWHM, the fastest response time yet reported for a GaAs p-i-n diode. Figure 4-4 is a photomicrograph of the device. The large half-moon-shaped electrode provides electrical contact to the cathode. The mesa structure that contains the active layers is a semicircle with a 12- μm radius. The small semicircular ohmic contact to the anode, which has a radius of $\sim 6 \mu\text{m}$, is accessed by a large truncated electrode. The area not covered by metal is the ring-shaped 6- μm gap between the anode and cathode contacts. The surface of this photoactive area consists of the p-layer, through which the light has to pass in order to reach the depletion region. The measured junction capacitance was 12 fF, corresponding to a specific capacitance of 0.05 fF/ μm^2 . An additional parasitic capacitance of ~ 5 fF resulted from the metallic electrodes.

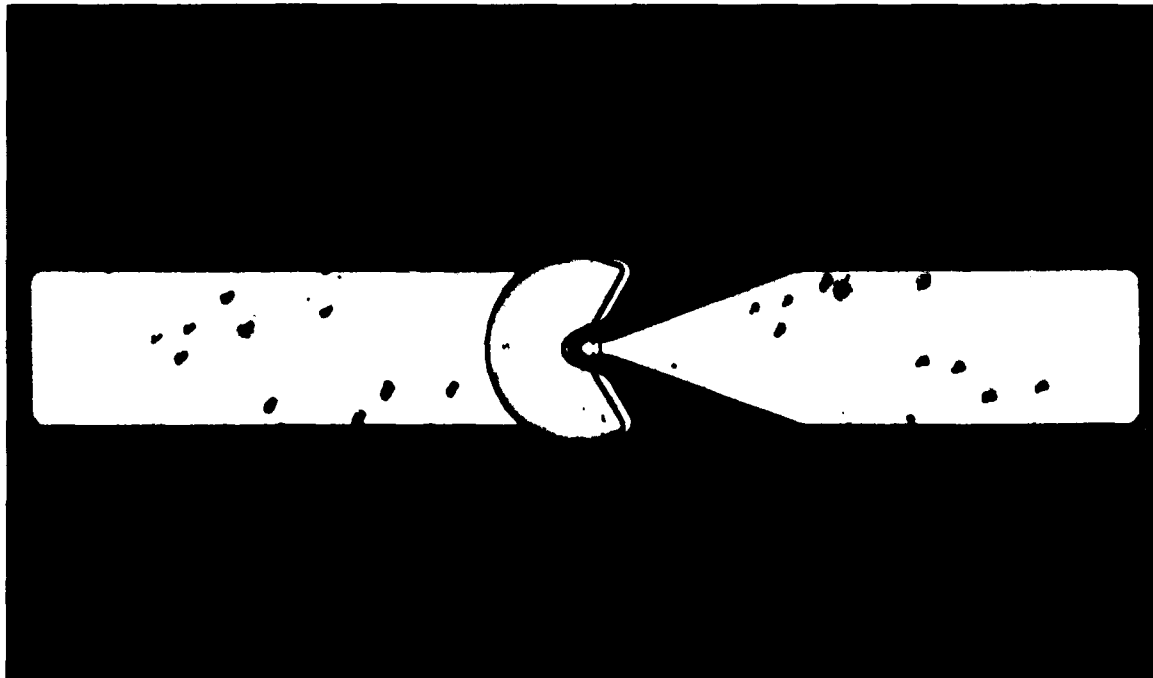


Figure 4-4. Photomicrograph of p-i-n device. Width of electrodes is 100 μm . This device was designed as an RF switch for microwave and millimeter-wave applications.

More definitive measurements of the external quantum efficiency have been performed. Two methods were used, both using the 4-ps dye laser pulses. In one case the number of carriers generated per pulse, as determined by integrating the impulse response obtained with the sampling oscilloscope (see Figure 4-15 of Reference 7), was divided by the number of photons per pulse, giving an external quantum efficiency of 15 percent. In the other case the average photocurrent was divided by the average incident optical power, giving a responsivity of 0.1 A/W, which corresponds to the same efficiency value. Measurements carried

out at wavelengths of both 757 and 814 nm gave the same results. The photocurrent increased linearly with increasing light intensity. The external quantum efficiency can be increased by two straightforward techniques: (1) application of an antireflection coating to the p-layer; (2) fabrication of the p-layer from $\text{Ga}_{1-x}\text{Al}_x\text{As}$ to form a transparent window for incident light of wavelengths above 750 nm (see Reference 8).

With a reverse bias voltage of 2 V across the 2- μm depletion region, the carrier sweep-out should be governed by the saturation velocity⁹ of $\sim 10^7$ cm/s, which corresponds to a transit time of ~ 20 ps through the intrinsic layer. This estimate, together with the measured low value of the junction capacitance, suggests that the observed impulse response of 19 ps is essentially determined by the carrier transit time. If so, the time response can be improved by reducing the thickness of the 2- μm -wide intrinsic layer.

W. Lenth

R.W. Mountain

A. Chu

D.J. Silversmith

L.J. Mahoney

W.E. Barch

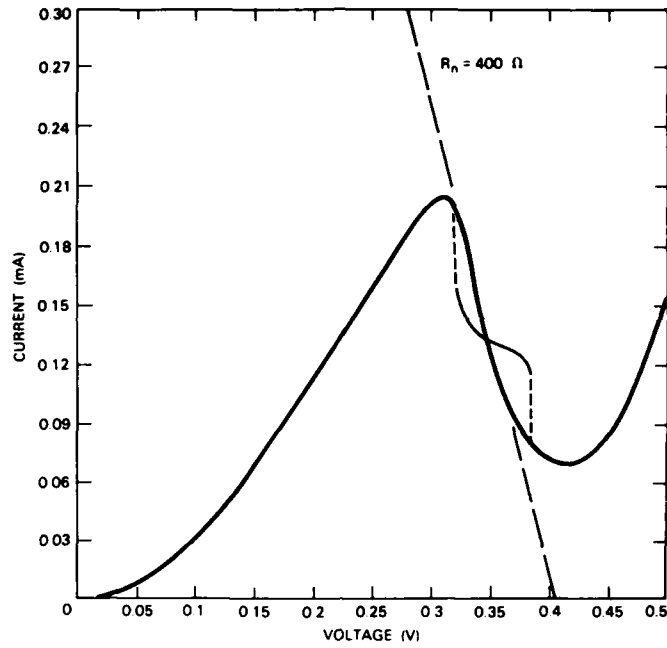
R.W. McClelland

4.3 QUANTUM WELL OSCILLATORS

Oscillations have been observed for the first time from double-barrier resonant tunneling structures. By eliminating impurities from the wells, we have been able to increase the tunneling current density by a factor of nearly 100 over previous devices.¹⁰ With the attendant increase in gain and improved impedance match to the resonant circuit, the devices oscillated readily in the negative resistance region. Oscillator output power of 5 μW and frequencies up to 18 GHz have been achieved with a DC-to-RF efficiency of 2.4 percent at temperatures as high as 200 K. The maximum observed frequency was limited by the coaxial circuit that conveniently served as the resonant structure rather than by the intrinsic time constants of the quantum well.

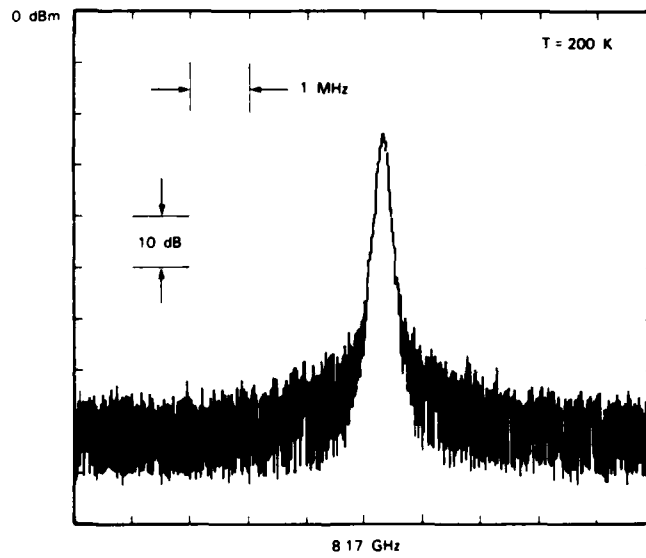
It is possible to damp the oscillations of devices with negative impedances of greater than a few hundred ohms by applying a broadband (0.1 to 18 GHz) 50- Ω termination. Figure 4-5 shows such an I-V curve traced out with the device at a temperature of 100 K. The dark curve shows the true I-V curve of the quantum well resonator; the light curve was taken when the device was oscillating at 4 GHz. The shift is due to the current response from self-detection of the oscillations. This interpretation is confirmed by the fact that the sign of the current response is the same as the curvature of the I-V curve, becoming zero at the inflection point. The dashed lines indicate the discontinuous transition between stable and oscillating states.

The spectrum of a quantum well resonator oscillating at 8.2 GHz and at a temperature of 200 K is shown in Figure 4-6. The bandwidth here is limited by the spectrum-analyzer resolution, but in measurements at higher resolution the bandwidth was limited by mechanical stability of the cavity to about 10 kHz. The wings 40 dB below the peak, which extend out to a few megahertz, are probably due to low-frequency noise mechanisms in the charge transport process.



142714-N-01

Figure 4-5. Current-voltage characteristic for a quantum well resonator. Dark line is true curve for a stable device; light line was measured when oscillating at 4 GHz. Difference is due to self-detection.



141500-R-01

Figure 4-6. Spectrum of oscillating quantum well resonator. Wings below -60 dBm which extend to a few megahertz are probably due to low-frequency noise in charge transport process.

The observed output in this case was 5 μ W. The maximum available power from such negative resistance devices is given by¹¹

$$P_{\max} = \frac{3}{16} \Delta V \Delta I \quad (4-1)$$

where $\Delta V(\Delta I)$ is the voltage (current) extent of the negative resistance. Then the maximum available power is 17 μ W. In view of the fact that no matching optimization has been attempted, this is reasonable agreement. The observed DC-to-RF efficiency is 2.4 percent, and the maximum efficiency based on Equation (4-1) would be about 8 percent.

Our calculations show that another factor-of-5 can be gained by a further reduction in scattering, and there is at least another factor-of-10 to be gained by changing barrier thicknesses.

If impedance levels get too low because of the higher current density, either a smaller diameter or a series-connected stack could be used. With these methods oscillation frequencies of a few hundred gigahertz could be achieved. The output power would also increase at higher current densities.

T.C.L.G. Sollner
P.E. Tannenwald

D.D. Peck
W.D. Goodhue

REFERENCES

1. Solid State Research Report, Lincoln Laboratory, M.I.T. (1984:3), p. 53.
2. I. Deyhimi, R.C. Eden, and J.S. Harris, IEEE Trans. Electron Devices **ED-27**, 1172 (1980).
3. U. Ablassmeier, W. Kellner, H. Herbst, and H. Kniepkamp, IEEE Trans. Electron Devices **ED-27**, 1181 (1980).
4. M.D. Clark, C.L. Anderson, R.A. Jullens, and G.S. Kamath, IEEE Trans. Electron Devices **ED-27**, 1183 (1980).
5. M.J. Cohen, IEEE International Electron Devices Meeting, Technical Digest, p. 622, December 1981.
6. G.L. Hansell, "GaAs Schottky-Barrier Charge-Coupled Devices," Ph.D. Dissertation, M.I.T. (June 1982).
7. Solid State Research Report, Lincoln Laboratory, M.I.T. (1984:1), p. 62, DTIC AD-A147429.
8. N. Bar-Chaim, K.Y. Lan, I. Ury, and A. Yariv, Appl. Phys. Lett. **43**, 261 (1983).
9. S.M. Sze, *Physics of Semiconductor Devices* (Wiley, New York, 1981), p. 46.
10. T.C.L.G. Sollner, W.D. Goodhue, P.E. Tannenwald, C.D. Parker, and D.D. Peck, Appl. Phys. Lett. **43**, 588 (1983), DTIC AD-A136442/1.
11. R.F. Trambarulo, International Solid-State Circuits Conference, Philadelphia, Pennsylvania, 1961.

5. ANALOG DEVICE TECHNOLOGY

5.1 HISTOGRAM READOUT TECHNIQUE FOR CHARGE-COUPLED IMAGE PROCESSORS

This report describes the initial experimental demonstration of a new readout technique for a charge-coupled device (CCD) image processor that provides a histogram of the distribution of pixel intensities in the image. Specifically, an output waveform is obtained whose amplitude represents the number of pixels in a selected part of the image whose intensity is greater than a value that is made to decrease linearly with time. Some examples of the use of such information would be to provide a means for establishing rapid dynamic threshold levels for an image digitizer or, when applied to the difference of two images, to indicate when a change has occurred in a scene.

To accomplish this function with conventional imagers one would have to digitize the entire image, store it in a computer, and then sort the pixel intensities into memory bins for each resolvable increment of intensity over the full intensity range. The method described here can produce this information for an arbitrarily large image array in a single readout operation that would take much less time than that required to form the image in the first place.

The technique is based on sensing current in an electrode which is common to all of the pixels to be analyzed. The readout is performed in such a way that the following features are realized:

- (1) The magnitude of the current from any pixel from which current is flowing is constant in time and equal to current from any other pixel.
- (2) The time at which the current from a given pixel starts (or stops) depends on the quantity of charge in that pixel

The first feature implies that the amplitude of the current represents the number of pixels that are contributing to the output; the second feature implies that image intensity values get mapped onto the time axis. For example, if pixels with a high intensity begin to contribute current to the electrode earlier than pixels with a low intensity, then time corresponds to a decreasing intensity threshold, and the magnitude of the current corresponds to the number of pixels with that intensity or more.

We have conceived of a number of techniques for achieving the two performance features specified above. One example uses the device structure shown in Figure 5-1. It is an array of imaging elements (of which only two are shown) biased by transparent storage electrodes connected to bus G_s and linked by transfer electrodes connected to bus G_t to output diffusions connected to bus D .

The operational waveforms are illustrated in Figure 5-2. The transfer gate bus G_t is held at a DC reference level. The image is formed by raising the bias on G_s to form a

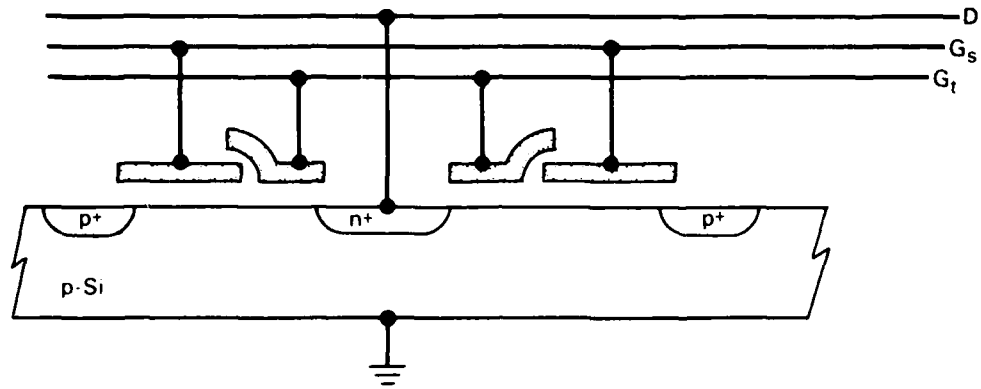


Figure 5-1. Example of a CCD structure for performing histogram readout.

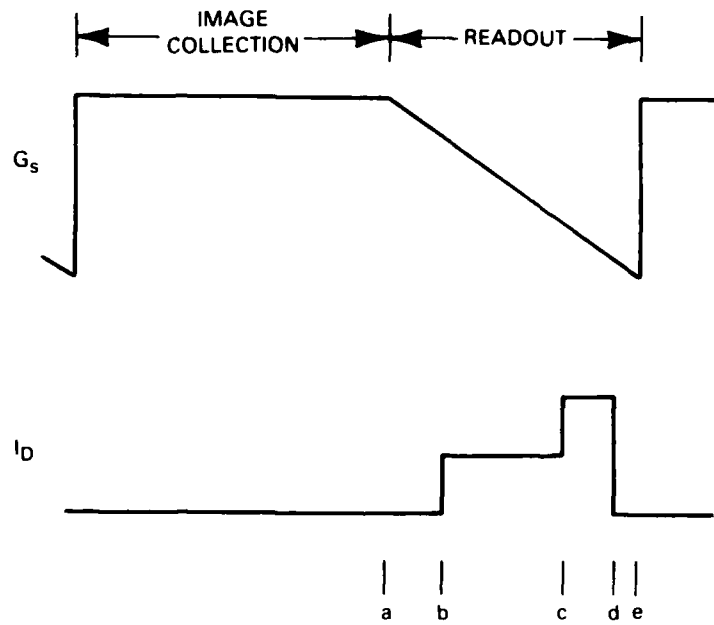


Figure 5-2. Drive waveform on storage gate G_s and output current I_D on common diffusion D during operation of histogram readout device.

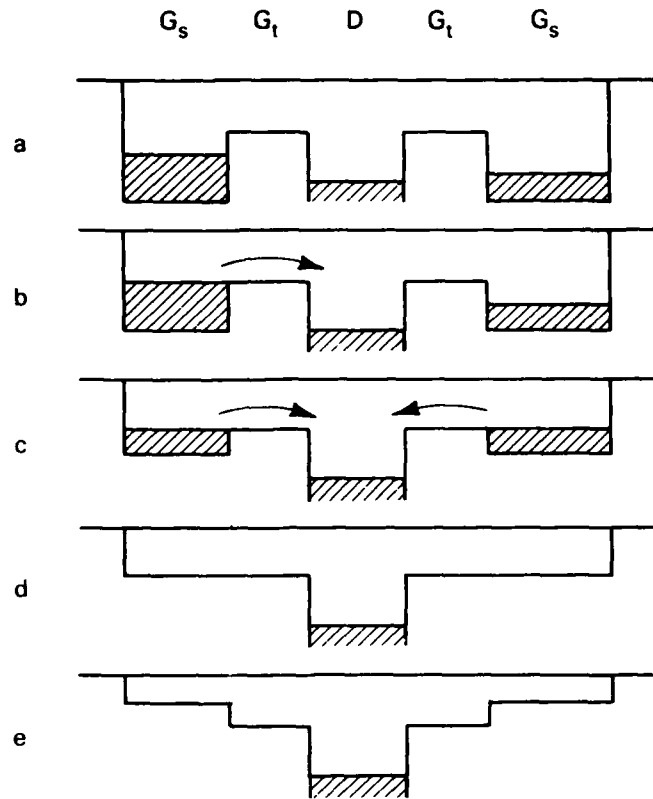


Figure 5-3. Charge-storage and flow patterns at times a through e shown in Figure 5-2.

depletion well under each storage electrode. Light enters these storage wells through the transparent electrodes and generates photoelectrons. After the photoelectrons are collected, each well contains a charge packet proportional to the light flux that was absorbed in that imaging element, as shown in Figure 5-3a.

After the image has been formed, the readout process begins. The indicated times a through e in Figure 5-2 correspond to the potential well and charge-storage patterns shown in Figures 5-3a through e. The bias on gate G_s is reduced linearly in time so that the floor of the potential wells rises. Initially, no current is collected on the output diffusion D. However, as soon as the potential floor has risen to the point shown in Figure 5-3b where the charge level in the fuller well is at the reference potential under gate G_t , then charge begins to spill over the transfer gate. The current collected on the output diffusion D from a single pixel is given by

$$I_{\text{pixel}} = C_{\text{ox}}(dV/dt)$$

where C_{ox} is the capacitance of the dielectric layer between gate G_s and the pixel cell, and dV/dt is the rate at which the bias on G_s is swept. As the voltage on gate G_s is further

reduced, the second pixel reaches the critical bias as shown in Figure 5-3c and begins to spill its charge across the transfer gate. With a linear ramp on G_s , the currents from each pixel will remain constant from the time they begin to flow until the floor of the pixel well reaches the reference level. Then the currents will drop abruptly to zero, as shown in Figure 5-3d.

The charge-spilling process occurs independently for each pixel in the imager, with the current starting to flow at a time inversely related to the charge in the pixel. The total current at time t is given by

$$I(t) = N[Q(t)] I_{\text{pixel}}$$

where $N[Q(t)]$ is the number of pixels with a charge packet greater than or equal to $Q(t)$, the amount of charge that produces a full well at the gate bias $G_s(t)$.

Figure 5-4 shows experimental results obtained using a CCD chip which includes a section with 32 wells connected via transfer gates to a common diffusion on one side and to a CCD shift register on the other. An electrical signal clocked in through the shift register provided a simulated image. This simulated image was made visible in the photographs in Figure 5-4 by clocking the 32-cell image through the register twice in each cycle. The first set of 32 charge packets passes through to the output from the serial register, where the charge packets are detected and appear as negative excursions from the baseline waveform in the middle traces in the photographs. The identical second set of 32 packets is transferred into the pixel wells when the voltage on G_s , shown in the upper traces in the photographs, is raised. The histogram readouts in the lower traces occur as the bias on G_s is ramped down.

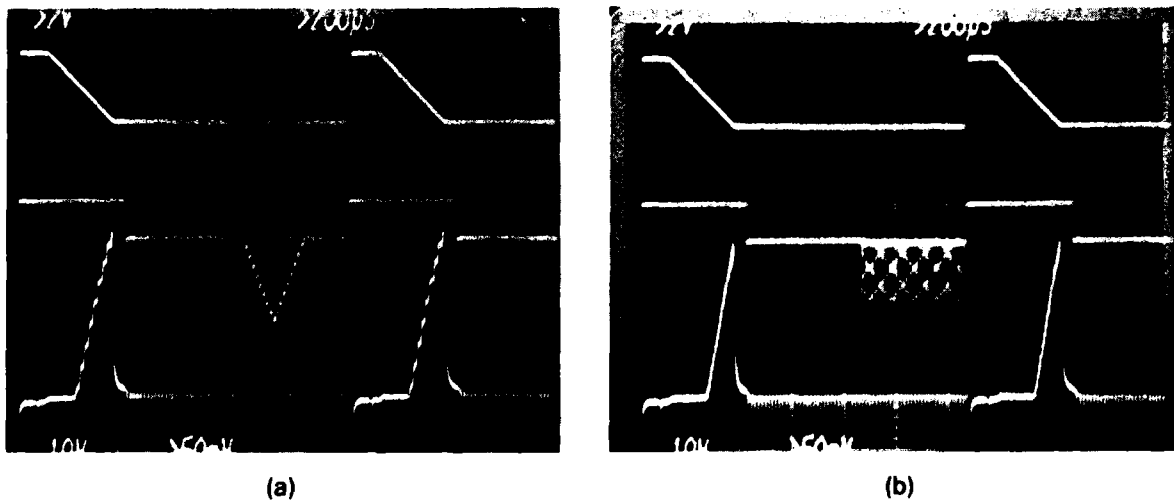


Figure 5-4. Experimental demonstration of histogram readout from a 32-well demonstration device for a steady (a) and shifting (b) triangular image pattern. Upper trace is voltage on G_s ; middle trace shows stored charge pattern (increasing downward); and bottom trace shows current on common diffusion D.

Figure 5-4(a) shows the histogram of a triangle pattern that was synchronized with the CCD clocks. The histogram shows the expected result. As the intensity threshold value sweeps down, it first picks up the peak of the triangle, and the histogram output jumps up one small division on the oscilloscope. Then the two next brightest pixels are reached, and the histogram output increases by two small divisions. The output continues to jump in two-division increments as progressively smaller pairs of pixels are included within the range of the threshold. Figure 5-4(b) shows a histogram for the same triangle pattern when it was not synchronized with the CCD clocks. The pattern is still the same, but it appears at a random position in the CCD and the precise sampling points on the triangle vary from scan to scan. The sharp transitions in the histogram are smeared out, and the result is the expected linear histogram.

The histogram information can also be read out using an optical beam rather than a ramped gate voltage. Consider again the condition shown in Figure 5-3a. Instead of raising the floor of the CCD wells by reducing the bias on G_s , we can shine a uniform beam of light onto the imager. All the pixels will begin to fill. When any pixel becomes filled to the level of the transfer gate, the photocurrent will begin to flow over the transfer gate and will be collected on the output diffusion (the diffusion and transfer gate regions are assumed to be shielded from light). The advantage of this readout technique over the electrical one described first is that the optical readout beam need not illuminate the entire imaging array, but can be directed onto any subset of pixels. It is then possible to obtain the histogram for any part of the image.

J.P. Sage

5.2 WIDEBAND SUPPRESSION OF STRONG SIGNALS IN THE PRESENCE OF WEAK SIGNALS BY BANDPASS-LIMITER CANCELLATION

In a communication receiver, a weak signal from a "far" transmitter can be unintentionally masked by the stronger signal from a "near" transmitter. This near/far problem is particularly troublesome when the two signal spectra are the same, as they would be in a dense network environment, and spectral excision of the interference is not possible. The problem has resulted in the favoring of FH (frequency-hopped) over PN (pseudonoise) systems because of the FH receiver's capability to provide >80 dB of rejection of tones adequately displaced in frequency from the desired tone, whereas a PN receiver's performance relies upon its processing gain which typically provides only 20 to 30 dB of rejection.

Although a PN receiver equipped with the capability to adaptively trade off data rate for processing gain provides some flexibility in near/far performance, it is not always acceptable to overcome a near/far problem by lowering the data rate. An alternate approach is to supplement the linear processing gain of a PN receiver with near/far adaptive cancellation circuitry. Adaptive cancellation is a signal-processing technique whereby the interference in a received waveform is estimated and this estimate is used to suppress the actual interference in the waveform by subtraction.

Described below is a bandpass-limiter cancellation technique; experimental results indicate that >30 dB of suppression of a high-level wideband signal relative to a low-level signal of equal bandwidth is possible using this process. The concept was demonstrated using minimum-shift-key (MSK) modulation of PN waveforms with 92.5-MHz chipping rates for both signal (low level) and interference (high level) and takes advantage of the constant-amplitude characteristic of such signals.

The realization of a practical adaptive cancellation technique for the near/far problem requires the derivation of a properly weighted interference estimate such that the residue of the interference in the received waveform, following subtraction, is small. Since such a cancellation process is additive, the signal component of the received waveform should remain undistorted, with no degradation to subsequent matched filtering.

When the interference in the received waveform is of constant amplitude, the 6-dB small-signal suppression effect of a bandpass limiter can be utilized to provide the desired interference estimate. A bandpass limiter consists of a limiting amplifier followed by a bandpass filter. The filter is designed to pass the signal spectrum while suppressing the harmonics that evolve from the limiting process. For received waveforms of reasonable signal-to-noise ratio, the small desired signal will be suppressed by 6 dB relative to the larger constant-amplitude interference when passed through a bandpass limiter.[†] The original phase is preserved in the bandpass-limited signal so that when this signal is properly normalized and subtracted from the received waveform, the large constant-amplitude interference is greatly suppressed while the small signal is reduced by only 6 dB, resulting in a net increase in the signal-to-interference ratio.

The amount of interference cancellation that can be obtained is dependent upon the amplitude and phase balance between the received waveform and its bandpass-limited version. In an actual circuit realization, the phase can be balanced by a one-time adjustment of the delay of the received waveform (prior to subtraction in a 180° hybrid) to take into account the signal delay through the bandpass-limiting circuitry. Because the output from the limiter is fixed in power, the power in the large signal following bandpass limiting is dependent upon the power in the conglomeration of all the lower-level signals. The amplitude of the bandpass-limited signal must therefore be dynamically adjusted depending upon the percentage of the power in the received waveform due to the strong signal component to be suppressed.

An important characteristic of this technique is that an interferer can be suppressed and the near/far tolerance of a PN receiver improved without the requirement for complex weight adjustment and the use of the least-mean-square (LMS) algorithm. A complex weight is obviated through careful gain and phase balance between the received waveform and the interference estimate.

Although only the largest constant-amplitude component of the received waveform can be canceled by this technique, stages may be cascaded in order to suppress a number of successively smaller interference terms.

[†] F.E. Nathanson, *Radar Design Principles* (McGraw-Hill, New York, 1969), pp. 119-124.

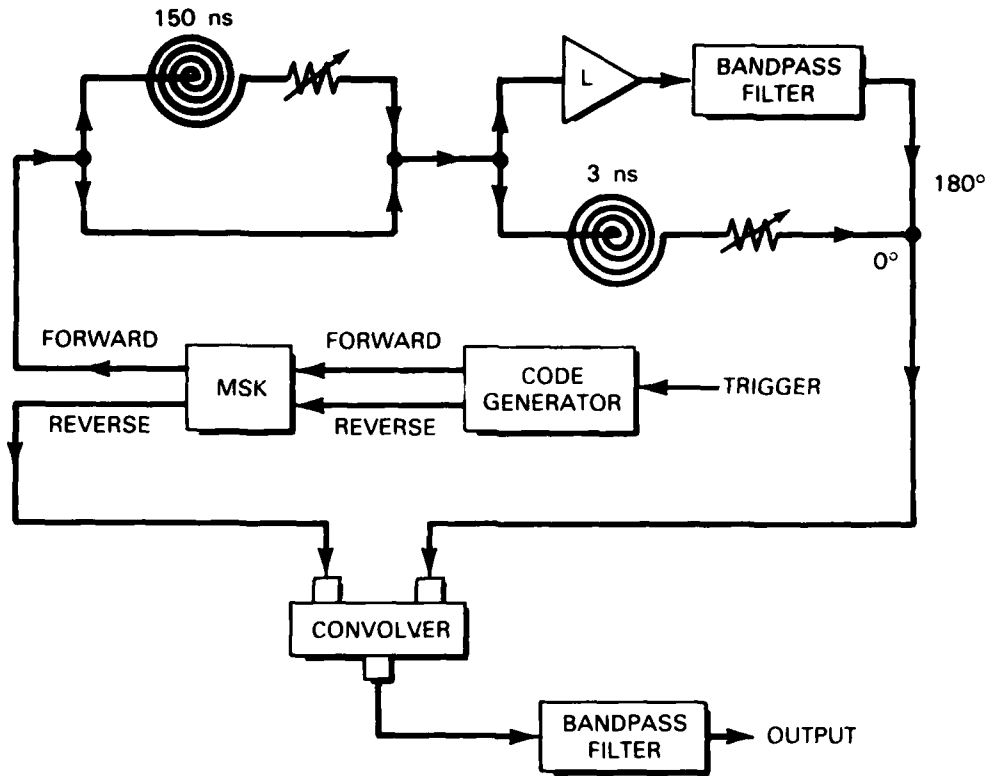


Figure 5-5. Larger (nearer) signal-suppression circuit.

The bandpass-limiter cancellation technique was demonstrated using both wideband and narrowband signals. Figure 5-5 shows the wideband demonstration where a PN code generator, running at a 92.5-MHz chip rate, was used to generate constantly changing forward and reverse code patterns of 1000 chips. These patterns were MSK modulated at a center frequency of 300 MHz, and the MSK-modulated reverse code was sent to one port of a SAW (surface-acoustic-wave) convolver so that this device could function as a matched filter for the MSK-modulated forward code.[†] A signal representing the desired component with interference was then generated by splitting the MSK-modulated forward code, delaying and attenuating one of these signals, and then recombining the two. This resulted in a signal consisting of two superimposed MSK-modulated forward codes, a large one representing the strong/near interferer, and a smaller delayed replica representing the weak/far desired component. After passing through the bandpass-limiter cancellation circuitry, this combined signal (when processed by the convolver matched filter) produced a correlation spike for both signals, with the spike for the smaller signal delayed relative to that produced by the larger signal. Such a signal was used so that the effect of the bandpass-limiter cancellation circuitry on both of the signals could be easily observed. In a real-life situation, the smaller signal would generally have no particular relationship to the larger one.

[†] Solid State Research Report, Lincoln Laboratory, M.I.T. (1984:1), p. 67, DTIC AD-A147429.

Figure 5-5 shows a 2-ft length (3 ns) of coaxial cable and an attenuator in the direct path of the canceler which were used to adjust the amplitude and phase balance between the two paths. The two correlation spikes for the signal and interference can be seen in Figure 5-6. Trace (a) was obtained by disabling the bandpass-limiter or reference leg of the canceler, while trace (b) was obtained by disabling the direct path. Note from this figure that, as is necessary for cancellation, the larger components are equal while the smaller component has been suppressed by 6 dB due to bandpass limiting. Trace (c) is the convolver output with both paths enabled. Clearly, the larger component has been significantly suppressed. Not only has the large spike been suppressed, but so have all of its side lobes.

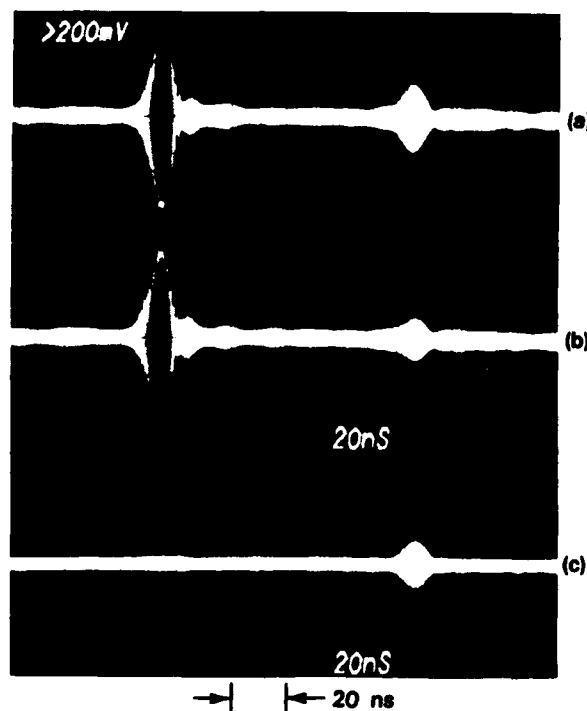


Figure 5-6. Near/far signal suppression results with two wideband input signals. Output of convolver matched filter is shown. (a) Output of convolver with bandpass-limiter path disabled and direct path enabled. (b) Output with bandpass-limiter leg enabled and direct path disabled. (c) Output with both circuit paths enabled. "Near" signal and its side lobes are clearly suppressed.

Finally, in order to demonstrate multiple cancellations, an additional delayed MSK component was added along with a second bandpass-limiter canceler cascaded with the first. Figure 5-7 shows the three resultant correlation spikes in trace (a). Trace (b) shows the suppression of the largest component when one canceler was enabled, while trace (c) shows the suppression of the two largest components when both cancelers were enabled.

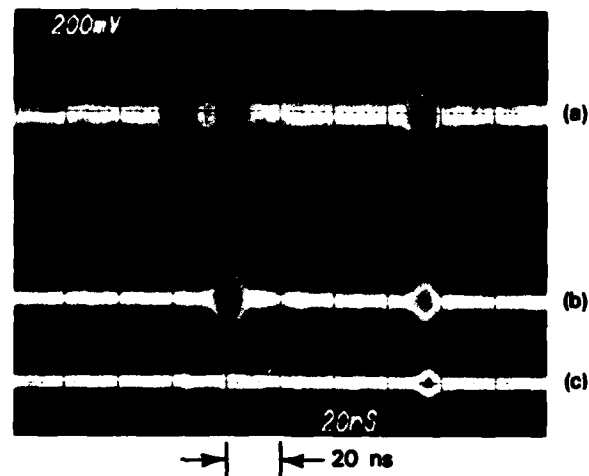


Figure 5-7. Multiple near/far suppression results. (a) Output for large and two successively smaller and delayed signals. (b) Output after a single stage of near/far suppression. (c) Output after two stages of near/far suppression.

A similar setup but with no matched filter was used for the narrowband demonstration. Two narrowband tones were summed and passed through the canceler, the output being observed on a spectrum analyzer. Figure 5-8(a) shows the spectral peaks due to the two tones with the bandpass-limiter leg of the circuit disabled. The two tones differ by about 20 dB. Figure 5-8(b) shows the result of tuned cancellation, providing about 50 dB of large tone cancellation with an expected 6 dB of small-signal suppression.

These results show that >30 dB of interference suppression is possible for a wideband signal such as the 92.5-MHz MSK-modulated PN signal used in the wideband demonstration. The narrowband results indicate that an even greater cancellation capability is possible for narrowband signals.

D.R. Arsenault
J.H. Cafarella

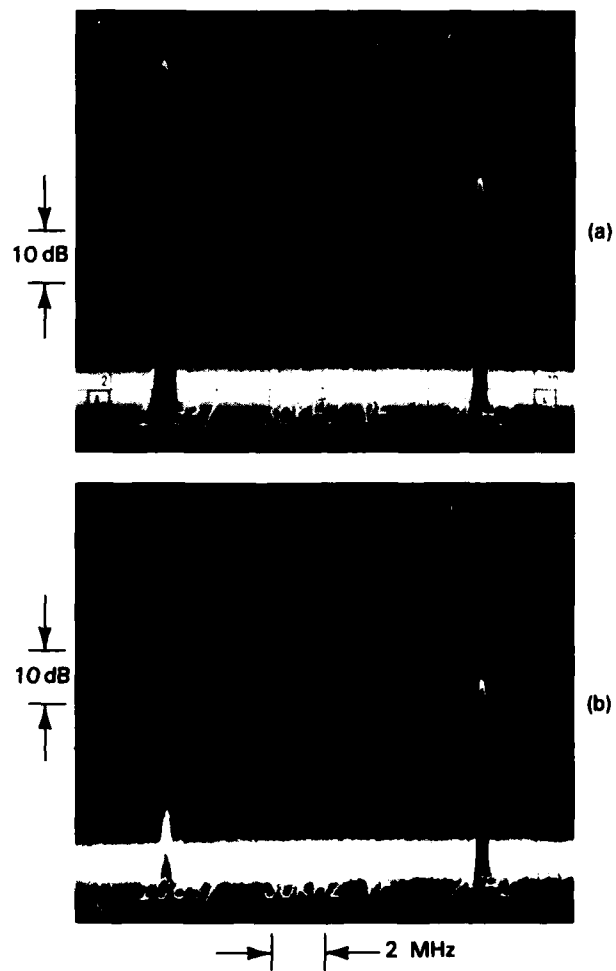


Figure 5-8. Narrowband near/far suppression results. (a) Spectrum of signal showing large and small narrow-band signals. Bandpass-limiter path is disabled. (b) Spectrum of signal with both paths enabled. Large tone is clearly suppressed.

148331-N

REPORT DOCUMENTATION PAGE		READ INSTRUCTIONS BEFORE COMPLETING FORM
1. REPORT NUMBER ESD-TR-84-295	2. GOVT ACCESSION NO. AD-A158013	3. RECIPIENT'S CATALOG NUMBER
4. TITLE (and Subtitle) Solid State Research		5. TYPE OF REPORT & PERIOD COVERED Quarterly Technical Report 1 August — 31 October 1984
		6. PERFORMING ORG. REPORT NUMBER 1984:4
7. AUTHOR(s) Alan L. McWhorter		8. CONTRACT OR GRANT NUMBER(s) F19628-85-C-0002
9. PERFORMING ORGANIZATION NAME AND ADDRESS Lincoln Laboratory, M.I.T. P.O. Box 73 Lexington, MA 02173-0073		10. PROGRAM ELEMENT, PROJECT, TASK AREA & WORK UNIT NUMBERS Program Element No. 63250F Project No. 649L
11. CONTROLLING OFFICE NAME AND ADDRESS Air Force Systems Command, USAF Andrews AFB Washington, DC 20334		12. REPORT DATE 15 November 1984
14. MONITORING AGENCY NAME & ADDRESS (if different from Controlling Office) Electronic Systems Division Hanscom AFB, MA 01731		13. NUMBER OF PAGES 80
		15. SECURITY CLASS. (of this report) Unclassified
16. DISTRIBUTION STATEMENT (of this Report) Approved for public release; distribution unlimited.		15a. DECLASSIFICATION DOWNGRADING SCHEDULE
17. DISTRIBUTION STATEMENT (of the abstract entered in Block 20, if different from Report)		
18. SUPPLEMENTARY NOTES None		
19. KEY WORDS (Continue on reverse side if necessary and identify by block number)		
solid state devices, quantum electronics, materials research, microelectronics, analog device technology,	photodiode devices, lasers, laser spectroscopy, imaging arrays, signal processing,	infrared imaging, surface-wave transducers, charge-coupled devices, acoustoelectric devices
20. ABSTRACT (Continue on reverse side if necessary and identify by block number)		
<p>This report covers in detail the solid state research work of the Solid State Division at Lincoln Laboratory for the period 1 August through 31 October 1984. The topics covered are Solid State Device Research, Quantum Electronics, Materials Research, Microelectronics, and Analog Device Technology. Funding is primarily provided by the Air Force, with additional support provided by the Army, DARPA, Navy, NASA, and DOE.</p>		

END

FILMED

10-85

DTIC